Ref. Ares(2023)8177922 - 30/11/2023

GO-VIKING

Research and Innovation Action (RIA)

This project has received funding from the Euratom research and innovation programme 2021-2025 under Grant Agreement No 101059603

Start date : 2022-06-01 Duration : 48 Months

Singlephase Cantilever rod experiment and benchmark setup

Authors : Dr. Hidajet HADZIC (Framatome GmbH), Andrea Cioncolini, Hao Li, Shanying Zhang, Mostafa Nabawy, and Hector Iacovides

GO-VIKING - Contract Number: 101059603

Project officer: Angelgiorgio IORIZZO

Document title	Singlephase Cantilever rod experiment and benchmark setup
Author(s)	Dr. Hidajet HADZIC, Andrea Cioncolini, Hao Li, Shanying Zhang, Mostafa Nabawy, and Hector Iacovides
Number of pages	70
Document type	Deliverable
Work Package	WP2
Document number	D2.1
Issued by	Framatome GmbH
Date of completion	2023-11-27 18:12:34
Dissemination level	Public

Summary

Description of the single phase experiment benchmark setup boundary conditions and experimental results

Approval

Date	By
2023-11-27 18:14:31	Dr. Hidajet HADZIC (Framatome GmbH)
2023-11-28 09:35:33	Dr. Papukchiev ANGEL (GRS)

WP2 – Flow-induced vibrations in fuel assemblies

Deliverable 2.1 of the GO-VIKING project (101060826) Single-phase cantilever rod experiment and benchmark setup

Version N°3.0
November / 2023

Hao Li, Andrea Cioncolini, Shanying Zhang, Hector Iacovides, and Mostafa Nabawy

Department of Fluids and Environment, The University of Manchester, M13 9PL Manchester, UK

Funded by
the European Union

Disclaimer

The content of this report reflects only the author's view. The European Commission is not responsible for any use that may be made of the information it contains.

Document information

Grant Agreement / Proposal ID	101060826
Project Title	Gathering expertise On Vibration ImpaKt In Nuclear power Generation
Project Acronym	GO-VIKING
Scientific Coordinator	Angel Papukchiev, mailto:Angel.Papukchiev@grs.de, GRS
Project starting date (duration)	1 June 2022 (48 Months)
Related Work Package	WP2
Related Task(s)	Task 2.1
Lead Organisation	University of Manchester (UoM)
Contributing Partner(s)	University of Manchester (UoM)
Due Date	Month 4
Submission Date	October 2022 for V1.0 December 2022 for V2.0 November 2023 for V3.0
Dissemination level	Do **NOT** release in public until conference and journal publications are released. These publications are expected to be released by end of 2024.

History

Date	Version	Submitted by	Reviewed by	Comments
October 2022	V1.0	UoM		
December 2022	V2.0	UoM		

November 2023	V3.0	UoM		Additional experiments performed for a variety of end pieces. Description and results hereof can be found in the additional journal paper draft attached to this deliverable as Appendix C.

Table of contents

1. General 8
2. GO-VIKING Research Objectives 8
3. Setup Description for the Single-Phase Cantilever Rod Experiment 8
3.1 Flow loop 8
3.2 Test section 9
3.3 Rod configuration 12
4. Data Collection 12
4.1 Motion tracking 12
4.2 Flow field visualisations 15
4.3 Flow conditions 16
5. Results 16
5.1 Rod vibration 16
5.2 Flow fields 18
6. Brief Summary of Outcomes 27
7. Data Requested 27
8. Appendix A 29
9. Appendix B 30
10. Appendix C 30

List of figures

Figure 1: Experimental test rig: (a) schematic of the two flow configurations; (b) real apparatus. 9

Figure 2: Experimental test section: (a) full test piece; (b) union cross internal configuration. Insert figure shows the internal structure of the flow straightener. 10

Figure 3: Rod end-piece dimensions. Hatching represents the rod pipe. 12

Figure 4: Motion tracking set-up arrangement. 13

Figure 5: Representative results for rod free vibration in still water. (a) Front displacement time-series; (b) Side displacement time-series; (c) Front displacement power spectrum (PDS); (d) Front displacement normalized histogram; (e) Front displacement autocorrelation (ATC); (f) Front displacement reconstructed attractor. 14

Figure 6: PIV set-up arrangement. 15

Figure 7: Rod vibration results. Left: Front displacements. Right: Side displacements. Upper: RMS displacement. Lower: Frequency. 17

Figure 8: Time-averaged contours of the normalised axial velocity, U, and turbulent shear stress u'v' (Uref is the mean velocity) over a section 10D upstream of the rod for Reynolds number of 70k. 18

Figure 9: Streamwise averaged profiles of the normalised velocity and turbulent shear stress (Uref is the mean velocity) at a location 10D upstream of the rod for a range of Reynolds numbers. 19

Figure 10: Time-averaged contours of the normalised axial mean velocity, U, radial mean velocity, V, normal turbulent stresses in the axial and radial directions, u'u' and v'v' respectively and turbulent shear stresses, u'v', (Uref is the mean velocity), for up flow at a Reynolds number of 20k. 19

Figure 11: Time-averaged contours of the normalised axial velocity and vector field for up-flow at a Reynolds number of 20k. 20

Figure 12: Time-averaged contours of the normalised axial mean velocity, U, radial mean velocity, V, normal turbulent stresses in the axial and radial directions, u'u' and v'v' respectively and turbulent shear stresses, u'v', (Uref is the mean velocity), for up flow at a Reynolds number of 40k. 20

Figure 13: Time-averaged contours of the normalised axial velocity and vector field for up-flow at a Reynolds number of 40k. 21

Figure 14: Time-averaged contours of the normalised axial mean velocity, U, radial mean velocity, V, normal turbulent stresses in the axial and radial directions, u'u' and v'v'

respectively and turbulent shear stresses, u'v', (Uref is the mean velocity), for up-flow at a Reynolds number of 80k. 21

Figure 15: Time-averaged contours of the normalised axial velocity and vector field for up-flow at a Reynolds number of 80k. 22

Figure 16: Time-averaged contours of the normalised axial mean velocity, U, radial mean velocity, V, normal turbulent stresses in the axial and radial directions, u'u' and v'v' respectively and turbulent shear stresses, u'v', (Uref is the mean velocity), for down-flow at a Reynolds number of 15k. 23

Figure 17: Time-averaged contours of the normalised axial velocity and vector field for down-flow at a Reynolds number of 15k. 23

Figure 18: Time-averaged contours of the normalised axial mean velocity, U, radial mean velocity, V, normal turbulent stresses in the axial and radial directions, u'u' and v'v' respectively and turbulent shear stresses, u'v', (Uref is the mean velocity), for down-flow at a Reynolds number of 20k. 24

Figure 19: Time-averaged contours of the normalised axial velocity and vector field for down-flow at a Reynolds number of 20k. 24

Figure 20: Time-averaged contours of the normalised axial mean velocity, U, radial mean velocity, V, normal turbulent stresses in the axial and radial directions, u'u' and v'v' respectively and turbulent shear stresses, u'v', (Uref is the mean velocity), for down-flow at a Reynolds number of 29k. 25

Figure 21: Time-averaged contours of the normalised axial velocity and vector field for down-flow at a Reynolds number of 29k. 25

Figure 22: contours of axial and radial velocities with vector fields as well as vorticity and streamlines for the instantaneous vector field of the down-flow encountering the rod at the extreme right position, for a Reynolds number of 56k. 26

Figure 23: contours of axial and radial velocities with vector fields as well as vorticity and streamlines for the instantaneous vector field of the down-flow encountering the rod at the extreme left for a Reynolds number of 56k. 26

Figure 24: Comparison between present and previous data from Cioncolini et al. (2018). ... 28

Figure 25: Illustration of the rod fixed end boundary condition. 29

Figure 26: Free vibration in air: only front displacement was recorded; 200 fps recording frequency. Euler-Bernoulli mode-1 vibration frequency is 4.10 Hz. 30

Abbreviations and Acronyms

Acronym	description
FIV	Fluid-Induced Vibration
FSI	Fluid-Structure Interaction
GO-VIKING	Gathering expertise On Vibration ImpaKt In Nuclear power Generation
PIV	Particle Image Velocimetry
WP	Work-Package

Summary

The Flow Induced Vibrations (FIV) of a free-clamped rod exposed to axial water flow have been experimentally investigated, using a custom-made test piece which comprises a rod confined inside a tube. Both the vibrating rod and the confining tube are made of stainless steel: the rod is filled with lead, whereas the confining tube accommodates a transparent section for optical access. This provides a simple configuration, with dimensions and linear mass density chosen to be informative of water-cooled nuclear reactor fuel rods. Experiments have been carried out with water at ambient conditions flowing towards the rod free-end (free-clamped configuration) and also adopting the reverse configuration, where water flows away from the rod free-end (clamped-free configuration). During the experiments, the Reynolds number (based on the hydraulic diameter of the annulus formed by the rod and the confining tube) was varied between 5,000 and 80,000: a range that significantly extends the scope of existing data on axial-flow-induced vibration of free-clamped rods. Measurements have been carried out using non-contact techniques: fast video imaging has been used to track the motion of the rod, while Particle Image Velocimetry (PIV) has been employed to resolve the flow field. For the free-clamped configuration, flutter was evident at low Reynolds numbers, whereas buckling occurred at high enough Reynolds numbers. On the other hand, for the clamped-free configuration, flutter was only evident with no buckling taking place. For both configurations, as the displacement reaches around 0.2-0.3 mm, the slope of the RMS displacement vs Reynolds number curve increased sharply till, for the free-clamped configuration, the rod buckles touching the confining tube and remain almost still in a deflected configuration, whereas for the clamped-free configuration, the rod continues to vibrate and does not buckle. PIV measurements exposed associated flow field features for interesting cases. In particular, the clamped-free configuration demonstrated a clear separation region behind the tip of the rod which was not evident for the free-clamped configuration. Since both the rod vibration and the flow field are monitored, the present data are particularly suited for development of numerical models and code validation.

Keywords

Axial flow; Vibration; Free-clamped rod; Experiment

1. General

D2.1 is concerned with providing a description of the single-phase experiment, benchmark setup, boundary conditions, and experimental results. This document describes the experimental setup used for the single-phase experiments, explains the conducted measurements for motion tracking and flow field visualisations, and presents the obtained experimental results.

2. GO-VIKING Research Objectives

The overall objective of GO-VIKING is to increase the expertise and improve the tools and skills of the European nuclear stakeholders in the analysis of complex FIV phenomena. This will maintain and further enhance nuclear plant operation and safety.

This will be accomplished by:

- **Generation of high-resolution numerical and experimental data of FIV in single and multiphase flows**
- **Development and validation of high- and medium-resolution, as well as fast-running practical tools for the FIV analysis**
- **Implementation of efficient methods for uncertainty propagation in the FIV analysis results**
- **Synthesis of best practice guidelines for FIV analysis in accordance with the needs of the stakeholders**
- **Targeted training of graduates and young experts as well as practitioners from stakeholders in FIV analysis and modelling techniques**

The GO-VIKING project will improve the safety of contemporary reactors and the design evaluation of new concepts by making available new experimental results and improved numerical approaches for the evaluation of FIV.

3. Setup Description for the Single-Phase Cantilever Rod Experiment

3.1 Flow loop

A schematic as well as a photograph of the flow loop are provided in Figure 1. The test rig represents an improved version from the rig used by Cioncolini et al. (2018): the test section is essentially the same, apart from a new transparent section, and the flow loop is conceptually analogous although realized with new, high-spec components. However, the novelty of the present investigation stems from a number of improvements implemented, including:

(1) measuring the clamped-free flow configuration which was not previously explored;

(2) investigation of a wider range of Reynolds number;

(3) 3D detection of the rod motion rather than 2D;

(4) a more advanced PIV setup.

The test section is connected to a recirculating open loop system driven by a pump (10HP Leeson pump; rotational speed: 3500 rpm). The test fluid is water, whose characteristics of density and viscosity are determined from its temperature, measured via a direct immersion digital thermometer (ETI-Electronic Temperature Measurements Ltd; Direct immersion aquarium thermometer; temperature range: 248–343 K; accuracy within ± 1 K). The mass flow rate is measured with a heavy-duty turbine flow meter (Cole-Parmer; flow rate range: 37.8–378 l/min; accuracy: ± 3.78 l/min) installed downstream of the pump and upstream of the test section. For flow rates that were too small for the turbine flow meter to resolve, these were measured with the mass weighting method: the flow at the outlet of the flow loop was collected in a bucket and its weight was divided by the collection time (accuracy: ± 5 %).

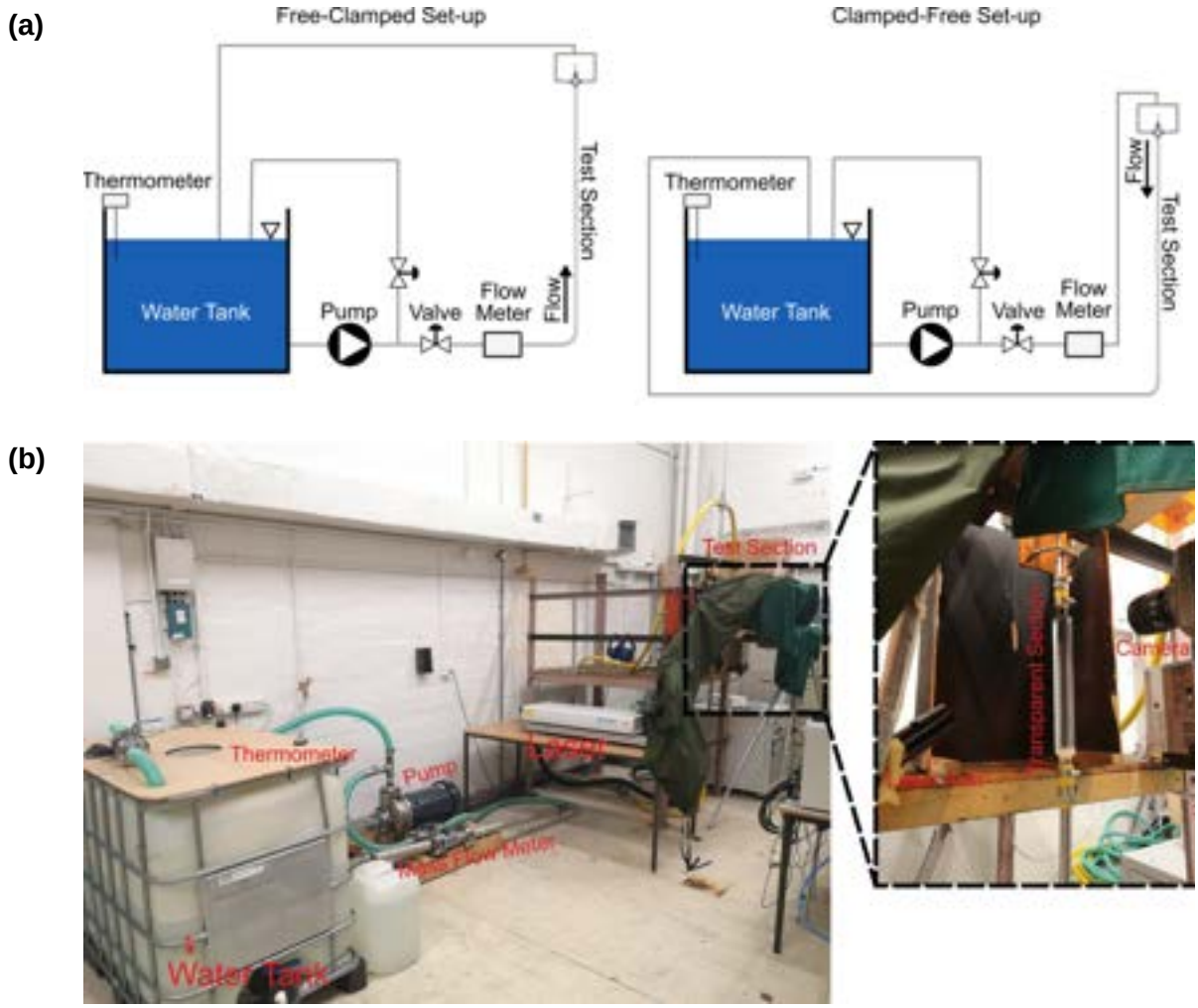

Figure 1: Experimental test rig: (a) schematic of the two flow configurations; (b) real apparatus.

3.2 Test section

A detailed schematic of the test section is shown in Figure 2. The test section has a vertical vibrating rod that is clamped at the top within a union cross and free at the bottom tip, where vibration takes place, inside a confining vertical tube. The flow can enter from either the top or bottom of the test section, see Figure 2, so that the test piece configures a simple rod-in-tube design with an axial annular flow that can be directed either upwards, impinging on the

free rod end and then moving along the annular section towards the fixed end, or downwards along the annular section, past the free rod end, exiting from the bottom end of the confining pipe.

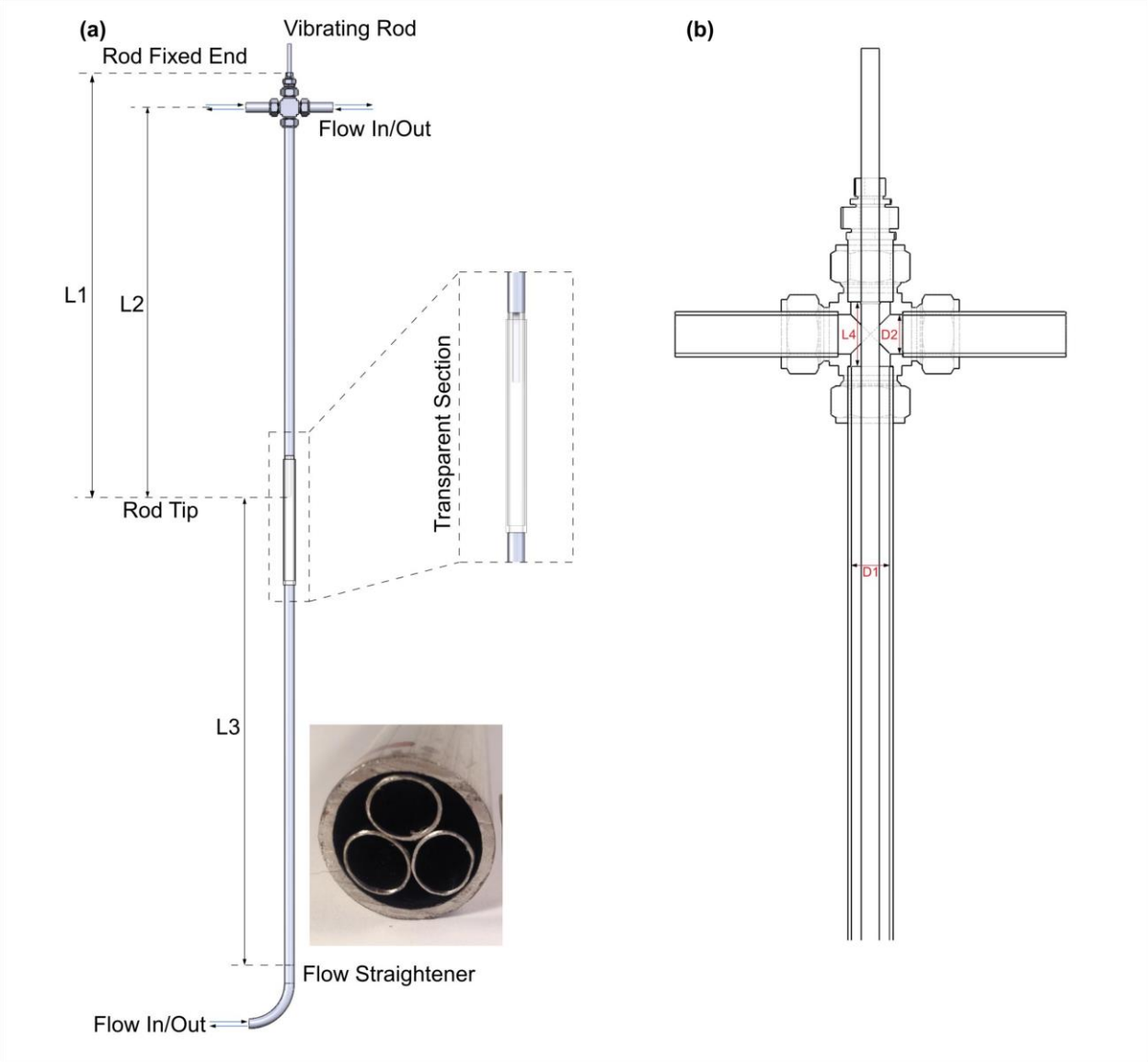

Figure 2: Experimental test section: (a) full test piece; (b) union cross internal configuration. Insert figure shows the internal structure of the flow straightener.

The confining pipe has 20.86±0.05 mm inner diameter (D1) and 25.06±0.01 mm outer diameter. The pipe is made of AISI 316 stainless steel and is rigidly connected to a fixed frame, attached to the rig. A matching diameter Perspex transparent section is inserted near the rod tip for optical detection of the rod motion and flow visualisation measurements. Because the flow is confined within a cylindrical tube, a surrounding rectangular box with flat faces was needed to reduce optical distortion via index matching. This surrounding structure has a square cross-section and is made of Perspex. The box structure was filled with water during experiments, which proved sufficient to remove the majority of the induced lensing effect of visualizing the flow through the cylindrical pipe.

A flow straightener is located at the bottom of the confining tube. For flows bottom-up, the flow passes through the straightener to remove swirl and secondary flows with limited pressure drop (straightener configuration is shown in the insert within Figure 2). The flow straightener is a tube-bundle conditioner comprising three pipes of the same nominal size as the vibrating rod piping (inner diameter of 8.83 ± 0.05 mm and outer diameter of 10.01 ± 0.06 mm), and with a length of 100 mm. Note that the three flow straightener pipes were mildly squashed to fit into the test section confining pipe. At the top, the test piece is connected to two symmetrically routed outlet pipes via a union cross (Swagelok SS-25M0-4; CAD of the union cross available from manufacturer[1]), which also holds the vibrating rod in place. A symmetric two-pipe configuration, rather than a standard one-pipe, was used to avoid any localised cross-flow close to the rod fixed-end, which could have affected the rod dynamics. Two symmetrically-routed pipes (same size as the test section confining tube, i.e. inner diameter of 20.86 ± 0.05 mm and outer diameter of 25.06 ± 0.01 mm), link to the branches of the union cross, which connects the test section to the flow loop.

As shown in Figure 2, the free length of the rod from the clamping point to the free end (L1) is 1045 ± 1 mm. The distance between the centre of the symmetric pipes and the free end of the rod (L2) is 944±1 mm; this dimension is provided as it can potentially assist with the definition of boundary conditions. Inside the union cross, the internal cross pipe section has diameter (D2) of 21.8 mm and length (L4) of 35.7 mm. Appendix A provides a more detailed illustration of the rod fixed-end boundary condition.

The test section has been operated in two different flow configurations, see Figure 2a. In the *free-clamped* flow configuration, the flow enters at the bottom of the test section and moves vertically upward from the rod free-end towards the clamped-end, finally leaving the test section at the top. The distance between the top of the flow straightener and the vibrating rod free end (L3) is 1100 mm, corresponding to a flow recovery length of 52.7 confining pipe diameters. As is shown later in the PIV measurements, the flow straightener and the flow recovery length are sufficient for the flow to approach fully-developed conditions upstream of the vibrating rod free-end.

In the *clamped-free* flow configuration, the flow enters at the top of the test section and then moves vertically downward from the rod clamped-end towards the free-end, finally leaving the test section at the bottom. In this case, the axial flow travelling along the vibrating rod results from the merging of the two incoming streams entering at the sides of the union cross (the two branches are symmetrically routed to avoid flow maldistribution): such a flow clearly depends on the mixing and directional change (from horizontal to vertical downward) of the two incoming streams, and it is comparatively less affected by upstream disturbances in the two feeding pipes. Hence, no flow straighteners were installed on the two feeding lines at the top of the test section. With the clamped-free flow configuration, the flow straightener installed at the bottom of the test section has clearly no effect on the flow travelling along the vibrating rod. The switching between the free-clamped and the clamped-free flow configurations was achieved by simply swapping the inlet and outlet connections between the flow loop and the test section.

[1] https://products.swagelok.com/en/c/tees/p/SS-25M0-3?q=SS-25M0

3.3 Rod configuration

The vibrating rod is made of an 8.83±0.05 mm/10.01±0.06 mm inner/outer diameter AISI 316 stainless steel circular tube (surface roughness = 2-3 µm). Hence, the hydraulic diameter of the annular gap between the confining tube and the vibrating rod is 10.85 mm (20.86 mm – 10.01 mm). The rod has a streamlined end-piece of semi-spherical shape, see Figure 3 for configuration and dimensions of the rod end-piece. To minimize any potential local mass effects of the end-piece on the rod dynamics, the semi-spherical end-piece was made of lightweight aluminium (density = 2.74 g.cm^{-3}) and has a mass of approximately 2.8 g (surface roughness = 0.4-0.5 µm) so that it does not appreciably alter the linear mass density of the vibrating rod. The vibrating rod was filled with lead shots (density: 11.34 g.cm^{-3}; diameters: 0.3-1.6 mm; source: manufacturer data) to mimic the loading of fuel pellets in nuclear fuel bundles. The measured mass density of the rod, accounting for rod material and lead shot filling, was 588 g.m^{-1}.

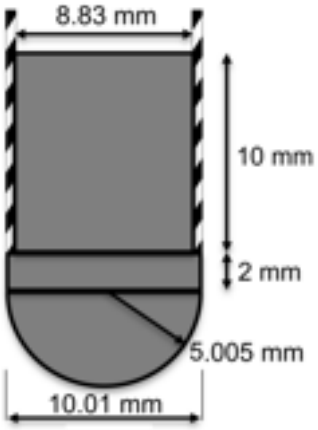

Figure 3: Rod end-piece dimensions. Hatching represents the rod pipe.

4. Data Collection

4.1 Motion tracking

The flow-induced motion of the free-end of the vibrating rod has been recorded using a fast-imaging camera (Panasonic Lumix DMC-FZ200; image resolution: 1280 x 720 pixels; recording frequency: 100 fps; recording duration: 60 s) positioned facing the test piece. The tip motion of the vibrating rod has been recorded from two sides, as a mirror placed at 45 degrees has been used so that both the front and side motions are captured, Figure 4. The recorded videos have been processed following common practice in image analysis: the recorded frames were converted to grey-scale, binarized and then complemented to isolate one single feature corresponding to the vibrating rod tip. The position of the rod tip centroid was computed and recorded to assemble the displacement time-series of the front and side motions which, once combined, characterise the rod motion in three dimensions. The image processing and the subsequent time-series analysis were carried out with the free software GNU Octave version 4.2.2 (Eaton et al, 2017), employing exclusively built-in features provided in the packages 'image' and 'signal'.

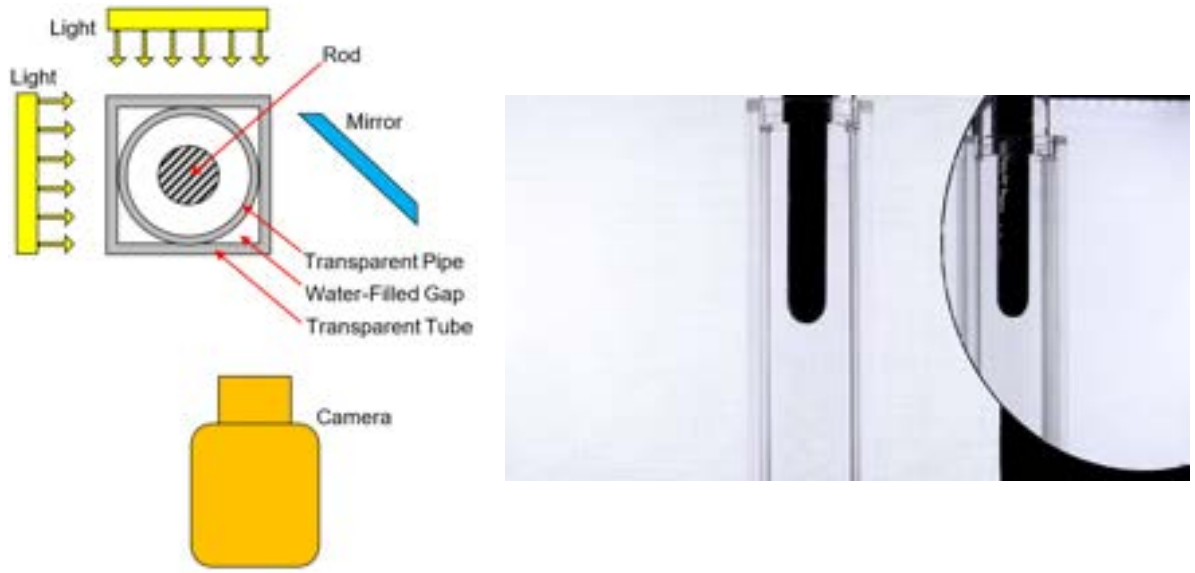

Figure 4: Motion tracking set-up arrangement.

The displacement time-series were characterised by computing their root-mean-square (RMS) values, and were further analysed by computing the power spectrum, the histogram, the autocorrelation function, and by reconstructing the attractor in phase-space. Before the analysis, the noise in the time-series was reduced using a 13-point Henderson moving-average filter. As is well known, moving average filters are effective at reducing noise in the time domain, but perform poorly in the frequency domain (Smith, 2003). Therefore, the power spectrum was computed from the raw, unfiltered time-series using the Welch method, whilst the filtered time-series were used to inform the rest of the analysis.

The experimental setup was validated with preliminary free vibration experiments in still water. These tests involved filling the test section with static water, manually displacing the rod from equilibrium and then recording and analysing the subsequent free vibration of the rod. A representative example is provided in Figure 5 which includes the front and side displacement time-series, the power spectrum (power spectral density-PSD), the histogram, the autocorrelation function (ATC), and the reconstructed attractor computed for the front displacement. Care was taken in manually displacing the rod along the direction perpendicular to the camera view, so as to trigger a free vibration confined in the plane perpendicular to the camera view. This is evident when comparing the displacement time-series in Figure 5a-b: the front displacement is about one order of magnitude larger than the side displacement, indicating that the free vibration is almost two-dimensional. Hence, only the front displacement is analysed here. As can be noted in Figure 5, the power spectrum presents one dominant peak that nicely matches the free vibration frequency (3.72 Hz) of the rod computed with classic Euler-Bernoulli elastic beam theory; the histogram is bridge-shaped; the autocorrelation function is decaying-periodic; and the attractor is a converging spiral. These features are typical of a damped periodic motion, which is what was expected in this case. The damping ratio, which was computed from the logarithmic decrement of the envelope of the front displacement time series, equals 0.015 ± 0.001. Appendix B provides some extra results for testing in air.

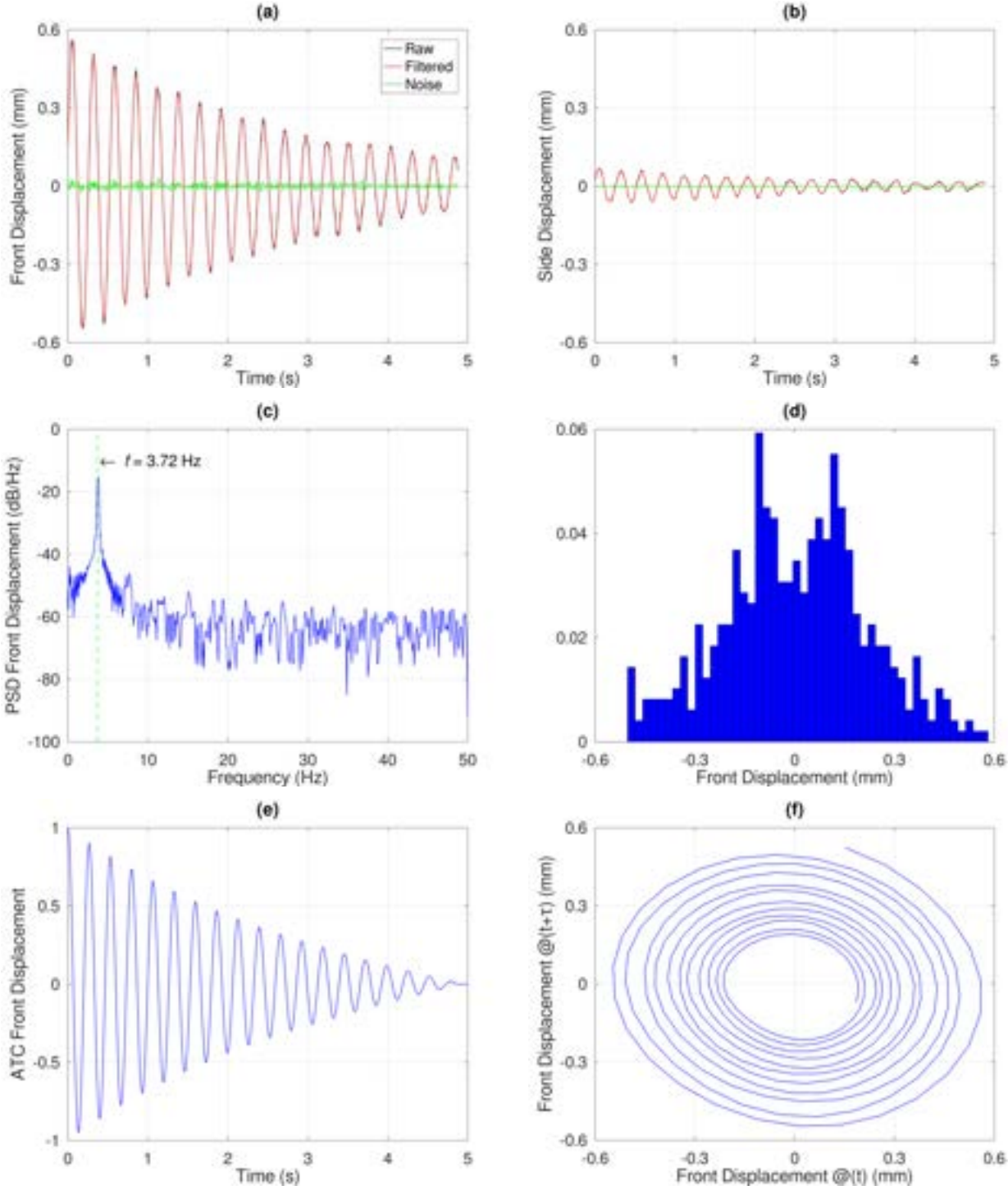

Figure 5: Representative results for rod free vibration in still water. (a) Front displacement time-series; (b) Side displacement time-series; (c) Front displacement power spectrum (PDS); (d) Front displacement normalized histogram; (e) Front displacement autocorrelation (ATC); (f) Front displacement reconstructed attractor.

Funded by
the European Union

4.2 Flow field visualisations

PIV measurements were carried out after the rod displacement data were acquired and analysed, and only at selected water flow rates, which were chosen to provide a comprehensive characterization of the flow field around the vibrating rod tip. Figure 6 below shows the PIV arrangement for investigating the flow-induced vibration at the transparent working section. A Dantec Dynamics PIV system was used in these measurements, consisting of a double cavity Nd:YLF laser, that provides maximum output energy of 15 mJ at a wavelength of 527nm. The laser was coupled to an articulated light arm with a beam-width-controlling optic and a divergent lens providing a two-dimensional vertical laser sheet across the centre plane of the flow field. The light sheet thickness was set by adjusting the distance between built-in lenses. The thickness of the laser sheet was approximately 1mm and the laser sheets were kept at angle to the flow direction so as to illuminate the flow field on both sides of the vibrating rod, hence avoiding the shadow of the rod obscuring part of the flow visualisation region, see Figure 6.

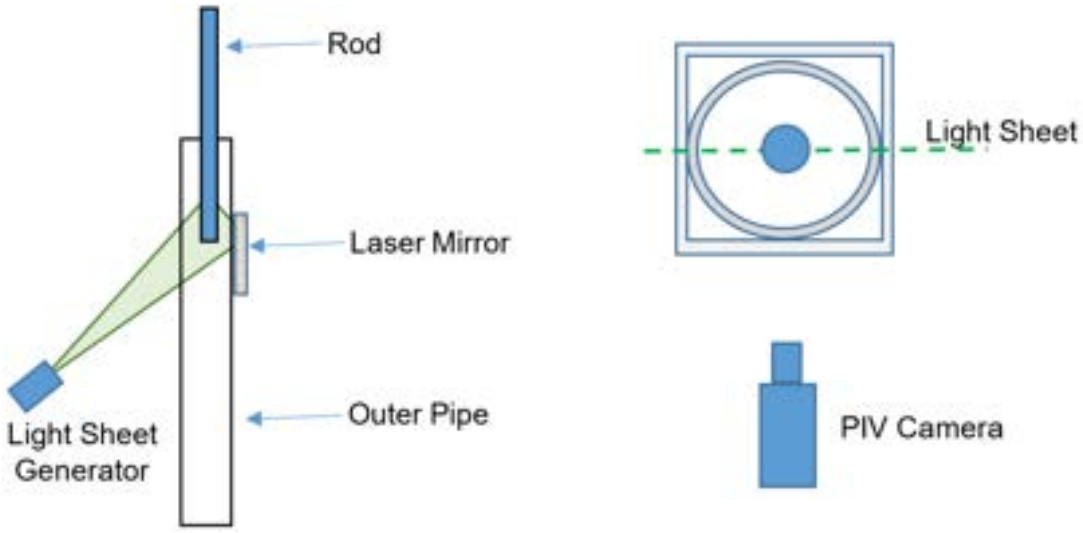

Figure 6: PIV set-up arrangement.

Recording of the seeding images on double frames was undertaken by using a high-speed camera (Phantom V310) running at 200 frames per second at 1280 x 800 full resolution using a Nikon AF Micro 60 *f/2.8D* lens. The velocity field mapping was generated from the displacement of particles seeded into the flow. Hollow glass spherical particles with a nominal size of 10 µm were selected for the current PIV measurements. These particles are small enough to follow the flow but large enough to generate bright light scattering for imaging. In addition, the size of these particles and their neutral density enable the trace particles to follow the flow correctly for accurate recording at a small interrogation area of PIV images. After adding the particles, the rig was left running at its highest flow rate for several minutes to circulate and evenly distribute the particles. To provide upstream conditions for up flows, another viewing window has been selected at approximately 10D (D: Diameter of the pipe) below the tip of the rod so as to ascertain the attainment of fully-developed pipe flow conditions upstream of the rod.

An important aspect of the measurement was to synchronise the laser pulses with the camera for the acquisition of the imaging in correct timing. Thus, Q-switch lased delay was used to

control the light pulse emission after each laser trigger. The separation times between pulses (50-200μs) have been set to have the maximum mean displacement in the plane of interest with a minimum loss of particles out of the plane.

Data have been obtained from 4108 pairs of images related to measurement planes in order to obtain the averaged velocity field and relevant statistics. The recorded images were processed by PIVLab code in MATLAB to calculate the velocity field for the plane under investigation. The image of the flow was divided into small areas known as interrogation windows. The interrogation window of the first image was correlated to its correspondent in the second image of the pair, hence showing a correlation peak at the most likely displacement location of the particles in each interrogation window. The size of each interrogation window was set to 32x32 pixels with 50% overlap to enhance the overall resolution. Each instantaneous image was cropped into a size of 1280×512 pixels to produce 79x31 instantaneous velocity vectors after correlation.

4.3 Flow conditions

The working fluid was tap water (tracking measurements took place at a temperature range of 17-23 ^{o}C; pressure was within 100-300 kPa, but the pressure value had no effect on the density and viscosity of water at the conditions explored). Water density and viscosity were calculated from measured temperatures using NIST-REFPROP. Both upward and downward flow directions were tested. The Reynolds number range in both directions was within 5,000-80,000 as estimated based on annulus mean flow velocity and annulus hydraulic diameter (10.85 mm). Approximately 100-200 videos were recorded for every flow direction (up/down) for the rod-motion-tracking part of the experiment. Indicatively, PIV measurements were obtained at several relevant Reynolds number values that lead to different dynamics.

5. Results

5.1 Rod vibration

The results for the rod vibration are provided in Figure 7, where the root-mean-square (RMS) displacement and the vibration frequency measured for the front and the side motions are presented as a function of the annulus Reynolds number (computed for the annular channel between the confining tube and the vibrating rod). Both flow configurations are included in Figure 7: the *free-clamped* (flow entering at the bottom of the test piece and directed upwards impinging on the free rod end, and then moving along the annular section towards the fixed end) and the *clamped-free* (flow entering at the top of the test piece and directed downwards along the annular section, past the free rod end). The vibration frequencies correspond to the dominant peaks in the power spectra of the rod displacement time series. With both flow configurations, the responses and associated dynamics deduced from the front and the side motions are analogous, both qualitatively and quantitatively.

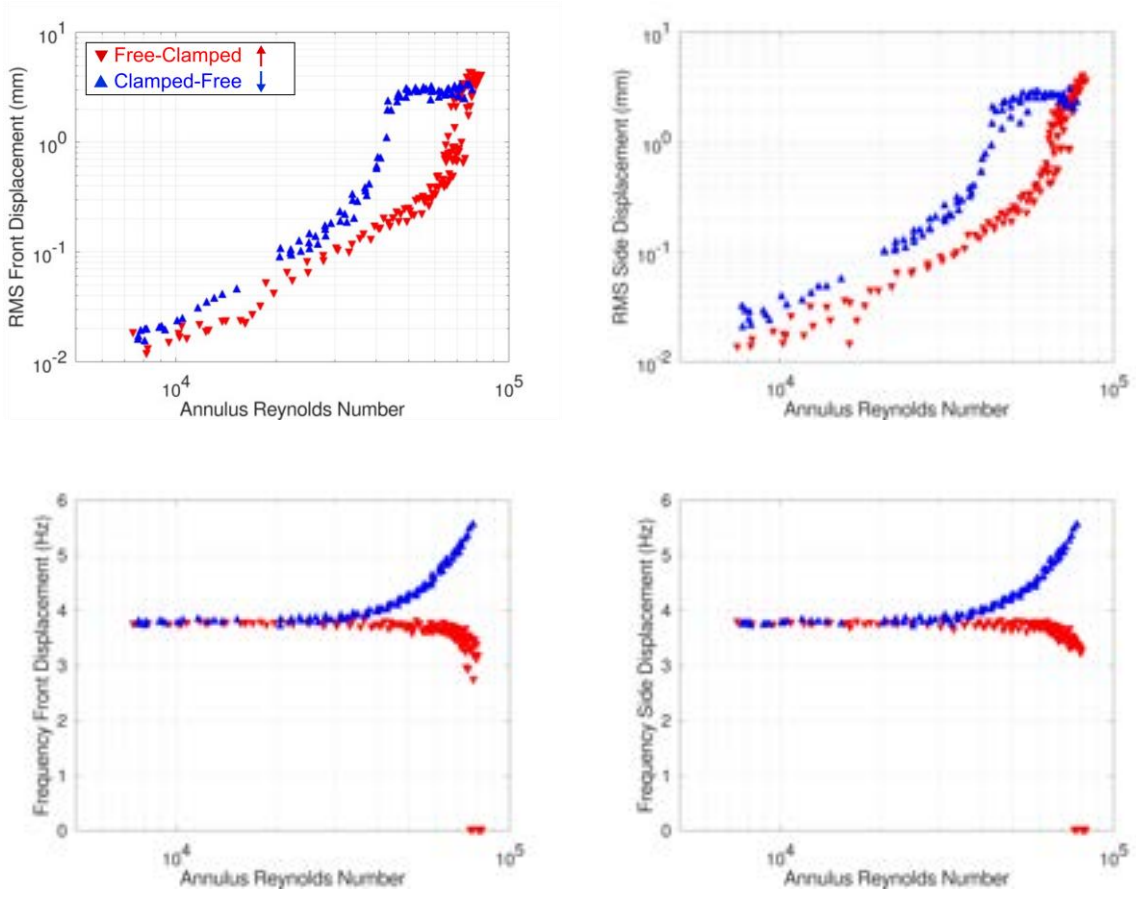

Figure 7: Rod vibration results. Left: Front displacements. Right: Side displacements. Upper: RMS displacement. Lower: Frequency.

Considering first the free-clamped configuration, the observed dynamics includes flutter at low values of the Reynolds number followed by buckling when the Reynolds number is large enough. At first, the RMS displacement increases when the flow velocity and consequently the annulus Reynolds number are increased. When the RMS displacement reaches values of around 0.2-0.3 mm, the slope of the RMS displacement vs. Reynolds number curve increases sharply until, upon further increase of the Reynolds number, the rod buckles touching the confining tube and remaining almost still in a deflected configuration. The vibration frequency correspondingly decreases until it reaches zero once the rod buckles and any periodicity in the rod vibration disappears (no dominant peaks in the power spectrum).

Regarding the clamped-free configuration, the observed dynamics only includes flutter, and buckling is not observed. As the Reynolds number is gradually increased the RMS displacement correspondingly increases. When the RMS displacement reaches values of around 0.2-0.3 mm, the slope of the RMS displacement vs. Reynolds number curve increases sharply until rod starts hitting the confining tube. The rod then continues to vibrate hitting the confining tube and does not buckle as observed with the free-clamped configuration. Note that the displacements provided in Figure 7 are RMS values, hence they do not saturate at a value corresponding to the maximum rod displacement corresponding to one-half the size of the annular gap (about 5.5mm). The vibration frequency gradually increases, indicating that once the rod vibrates hitting the confining tube the amplitude of motion does not increase

any longer whilst the vibration frequency gradually increases as the Reynolds number is further increased.

5.2 Flow fields

In this section, PIV results at indicative Reynolds numbers are presented. We start by showing results for up flows (flow going bottom-up) to establish flow conditions upstream of the rod for the free-clamped cases. Figure 8 shows the contours for the axial mean velocity and the turbulent shear stress over the section which is 10 diameters upstream of the tip of the rod, for a Reynolds number of 70k.

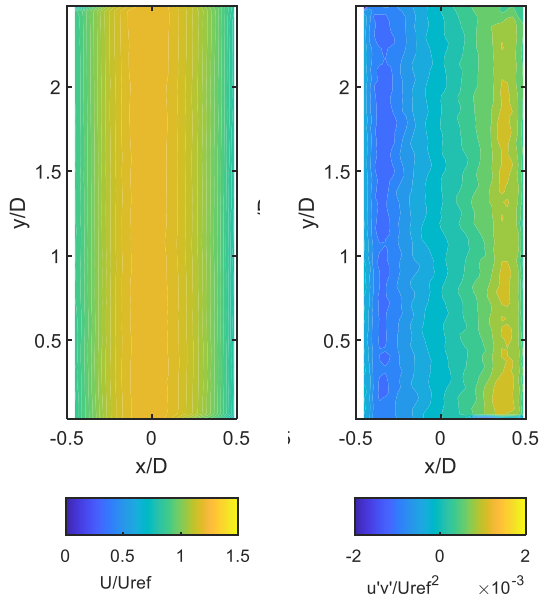

Figure 8: Time-averaged contours of the normalised axial velocity, U, and turbulent shear stress u'v' (Uref is the mean velocity) over a section 10D upstream of the rod for Reynolds number of 70k.

Sectional profiles have also been extracted and are shown in Figure 9, for Reynolds numbers ranging from 16k to 70k. Note that, to maintain consistency, the Reynolds numbers in Figures 8 and 9 are evaluated based on the annulus Reynolds number definition. The normalised profiles from the different Reynolds numbers, for both the mean velocity and the turbulent shear stress, collapse onto a single graph. Moreover, the turbulent shear stress shows a linear variation across the pipe. These comparisons confirm that for the free-clamped (upward flow) case, upstream of the rod end, flow conditions are close to those of fully developed pipe flow.

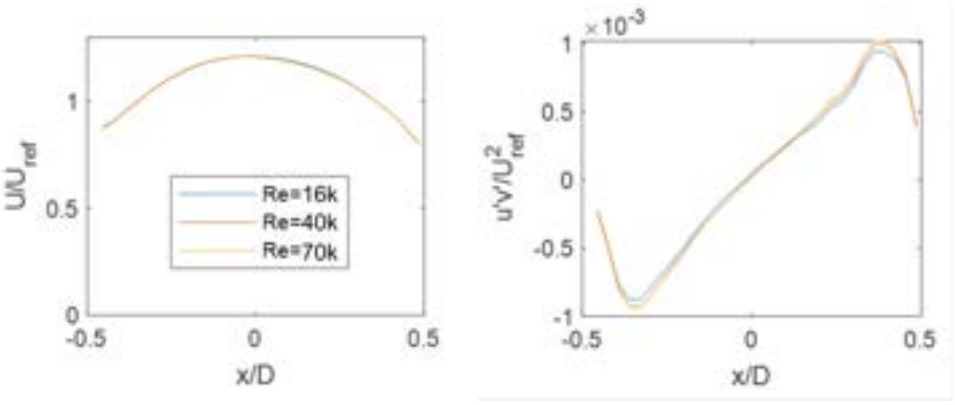

Figure 9: Streamwise averaged profiles of the normalised velocity and turbulent shear stress (Uref is the mean velocity) at a location 10D upstream of the rod for a range of Reynolds numbers.

For bottom-up flows encountering the tip of the rod creating the free-clamped configuration, Figure 10 shows the time-averaged contours of the axial and radial velocities as well as contours of the turbulent normal stresses in the axial and radial direction and the turbulent shear stress, near the tip of the rod for a Reynold number of 20k. The time-averaged flow fields show clear symmetry. The turbulent plot contours show that the highest turbulent levels over the tip of the rod, where there is flow impingement. The corresponding velocity field vector plots of Figure 11 confirm the symmetric character of the flow field and also highlight the flow acceleration that takes place as the flow is pushed into the annular passage. Plots for the higher Reynolds number cases, in Figures 12 to 15, show a similar flow pattern, but as the Reynolds number goes up, normalised turbulent levels around the end of the rod increase. This may be caused by the stronger impingement but also most likely by the vibration of the rod.

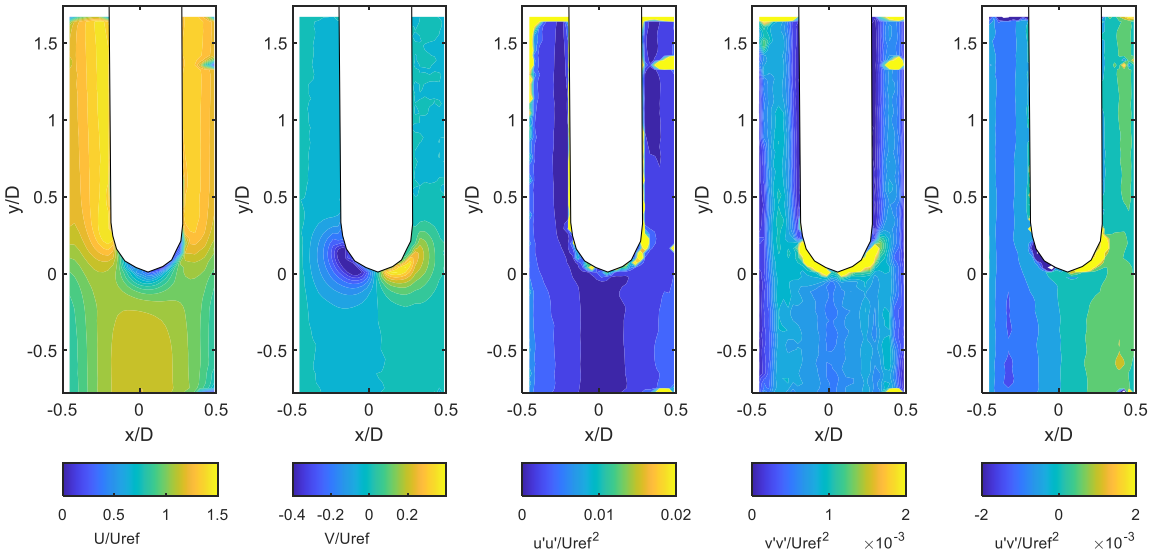

Figure 10: Time-averaged contours of the normalised axial mean velocity, U, radial mean velocity, V, normal turbulent stresses in the axial and radial directions, u'u' and v'v' respectively and turbulent shear stresses, u'v', (Uref is the mean velocity), for up flow at a Reynolds number of 20k.

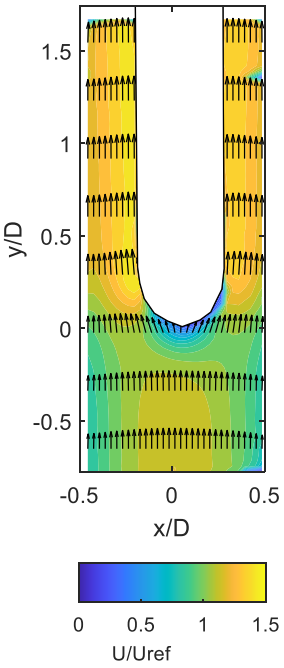

Figure 11: Time-averaged contours of the normalised axial velocity and vector field for up-flow at a Reynolds number of 20k.

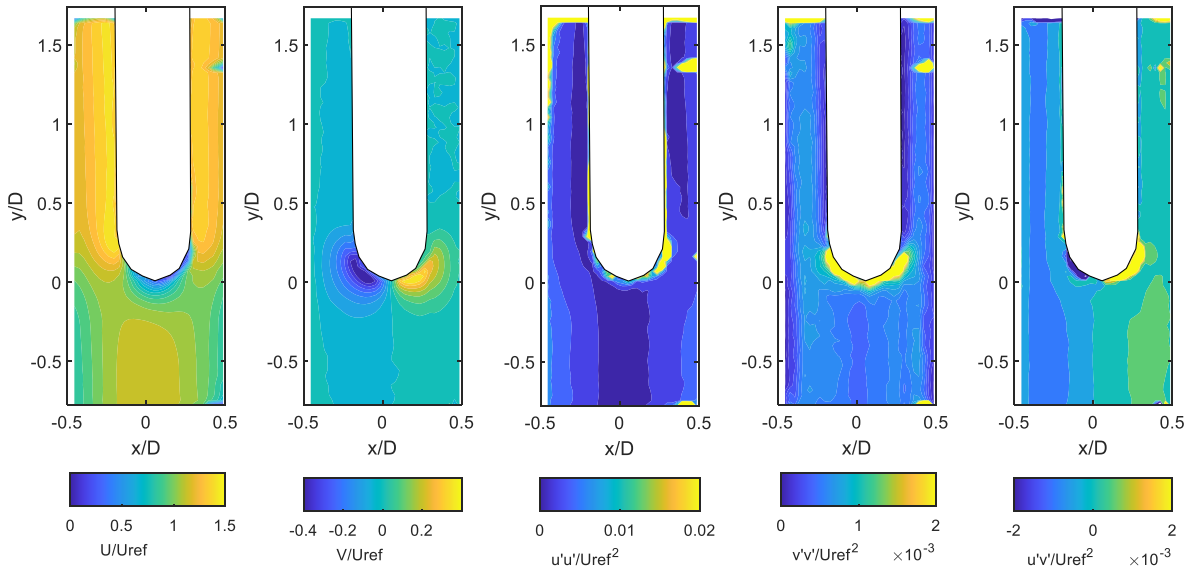

Figure 12: Time-averaged contours of the normalised axial mean velocity, U, radial mean velocity, V, normal turbulent stresses in the axial and radial directions, u'u' and v'v' respectively and turbulent shear stresses, u'v', (Uref is the mean velocity), for up flow at a Reynolds number of 40k.

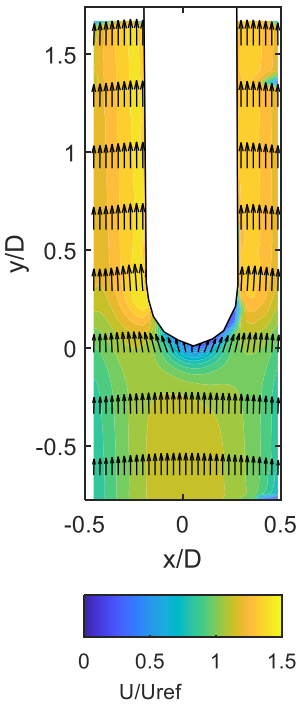

Figure 13: Time-averaged contours of the normalised axial velocity and vector field for up-flow at a Reynolds number of 40k.

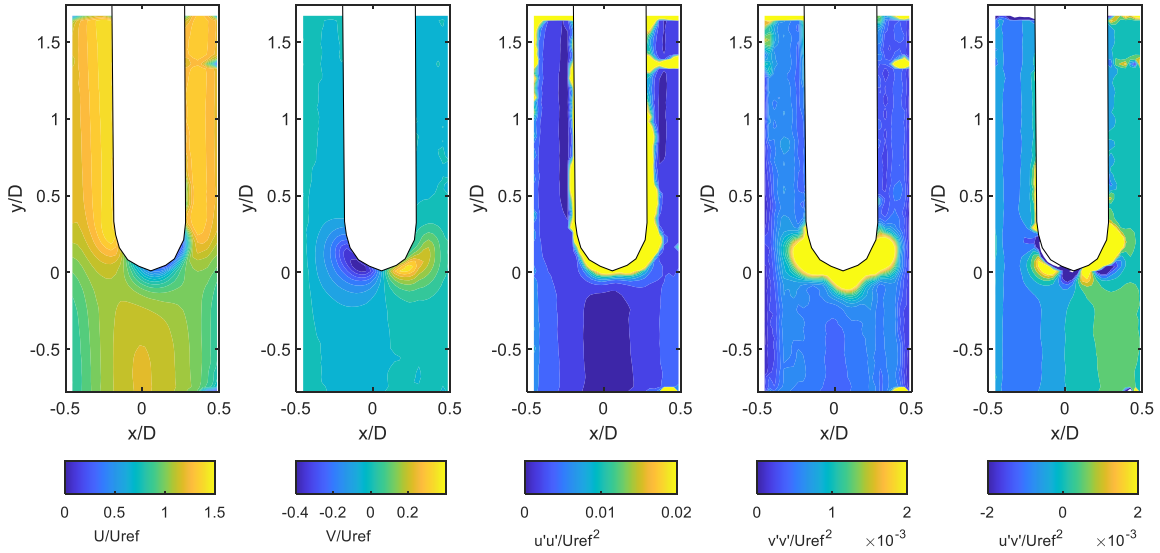

Figure 14: Time-averaged contours of the normalised axial mean velocity, U, radial mean velocity, V, normal turbulent stresses in the axial and radial directions, u'u' and v'v' respectively and turbulent shear stresses, u'v', (Uref is the mean velocity), for up-flow at a Reynolds number of 80k.

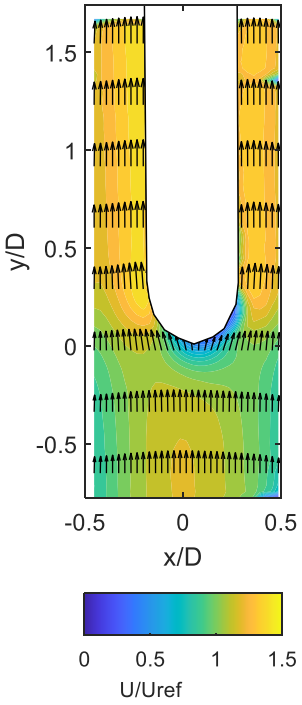

Figure 15: Time-averaged contours of the normalised axial velocity and vector field for up-flow at a Reynolds number of 80k.

For the top-down flows leading to the clamped-free configuration, Figure 16 shows the time-averaged contour plots of the normalised mean velocity components in the axial and radial directions, the turbulent normal stresses along the same directions and also the corresponding turbulent shear stress for a Reynolds number of 15k. As the flow moves from the annular section over the rod end and into the circular cross-section, it still retains its symmetric character, but now flow separates downstream of the rod, as demonstrated by the velocity field vector plot of Figure 17. Corresponding plots for higher Reynolds numbers, up to 29k, shown in Figures 18 to 21, suggest that up to a Reynolds number of 29k the downflow retains the same characteristics of flow symmetry and downstream wake.

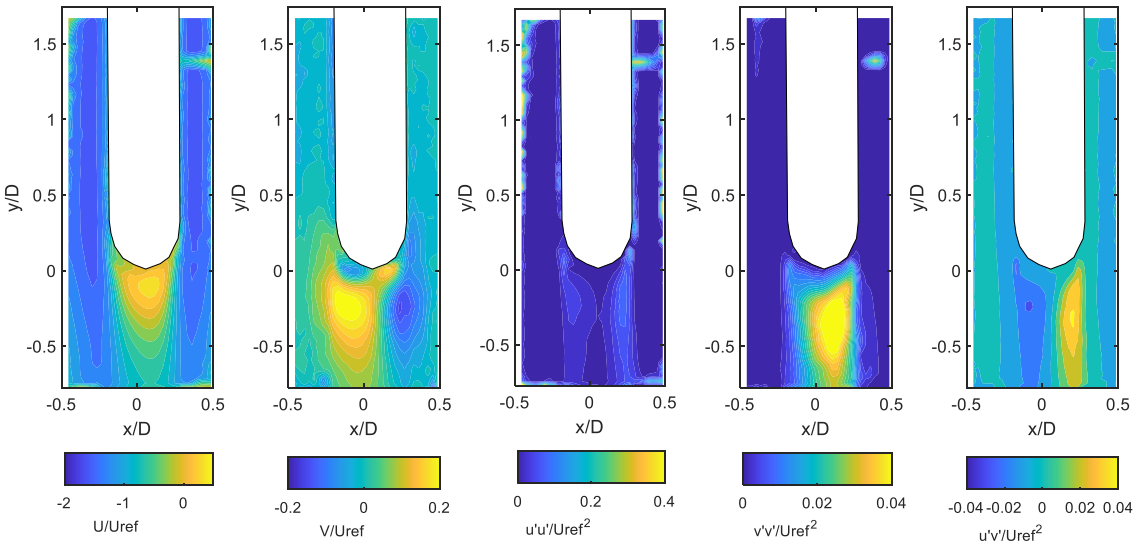

Figure 16: Time-averaged contours of the normalised axial mean velocity, U, radial mean velocity, V, normal turbulent stresses in the axial and radial directions, u'u' and v'v' respectively and turbulent shear stresses, u'v', (Uref is the mean velocity), for down-flow at a Reynolds number of 15k.

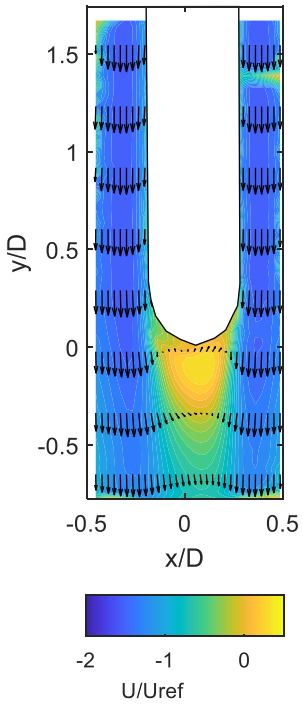

Figure 17: Time-averaged contours of the normalised axial velocity and vector field for down-flow at a Reynolds number of 15k.

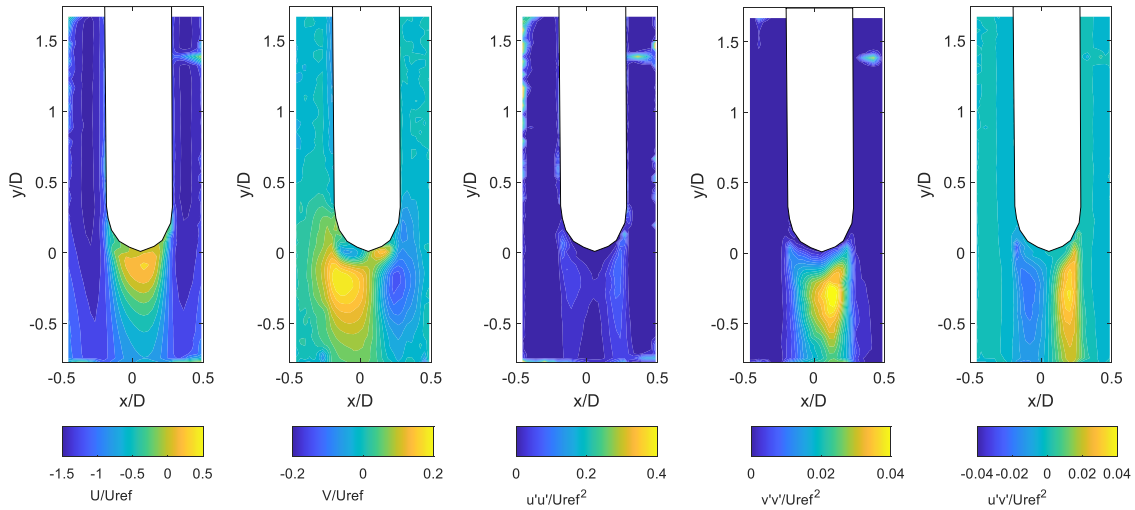

Figure 18: Time-averaged contours of the normalised axial mean velocity, U, radial mean velocity, V, normal turbulent stresses in the axial and radial directions, u'u' and v'v' respectively and turbulent shear stresses, u'v', (Uref is the mean velocity), for down-flow at a Reynolds number of 20k.

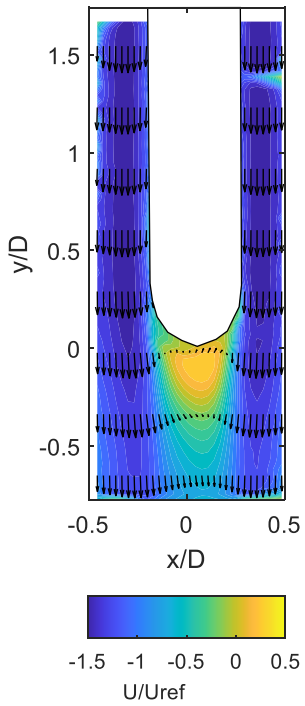

Figure 19: Time-averaged contours of the normalised axial velocity and vector field for down-flow at a Reynolds number of 20k.

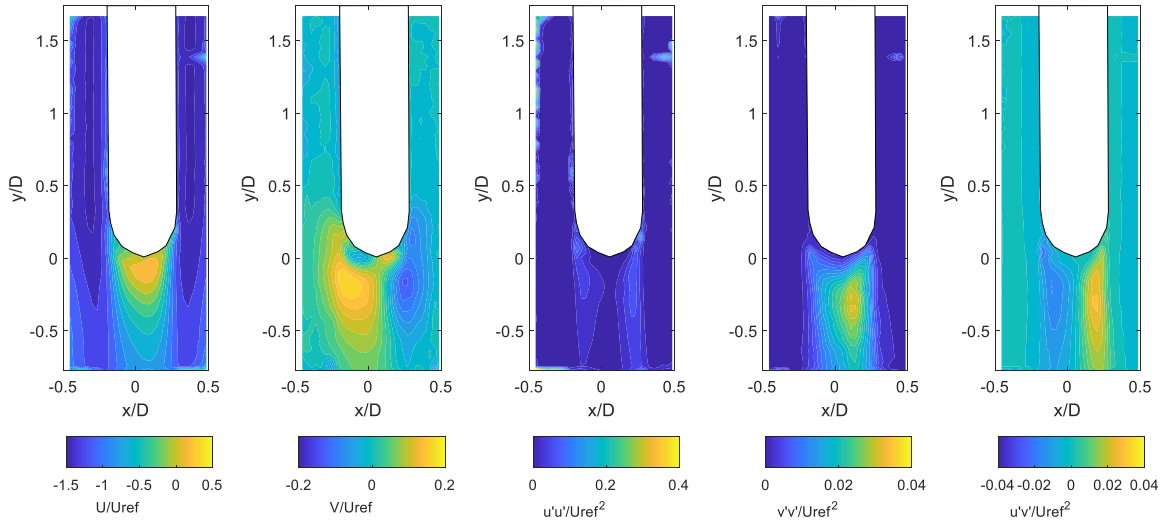

Figure 20: Time-averaged contours of the normalised axial mean velocity, U, radial mean velocity, V, normal turbulent stresses in the axial and radial directions, u'u' and v'v' respectively and turbulent shear stresses, u'v', (Uref is the mean velocity), for down-flow at a Reynolds number of 29k.

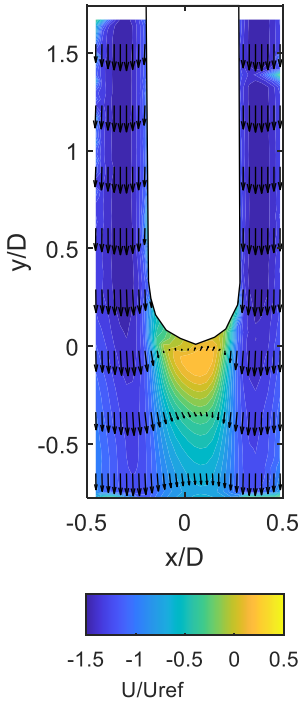

Figure 21: Time-averaged contours of the normalised axial velocity and vector field for down-flow at a Reynolds number of 29k.

For down-flows with Reynolds numbers higher than 29k, due to the large amplitude and three-dimensionality of the rod vibrations, time-averaged flow fields are no longer useful. Instead, results of two instantaneous velocity fields are presented in Figures 22 and 23. The flow before and after the rod tip is no longer symmetric and the flow separation region becomes more

extensive. For down-flow, the flow development around the rod tip is different and more complex than that for the up-flow.

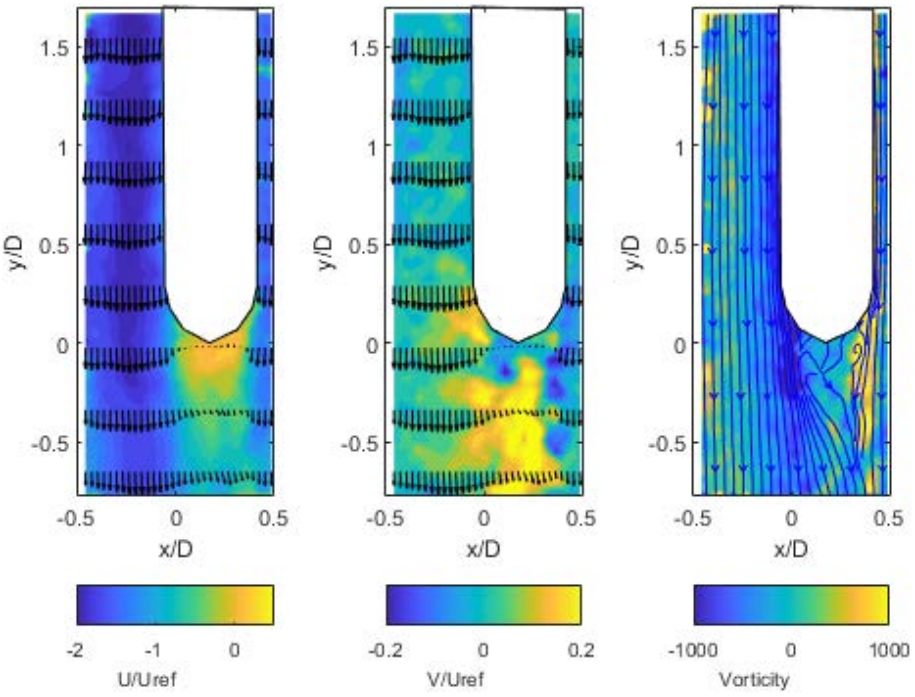

Figure 22: contours of axial and radial velocities with vector fields as well as vorticity and streamlines for the instantaneous vector field of the down-flow encountering the rod at the extreme right position, for a Reynolds number of 56k.

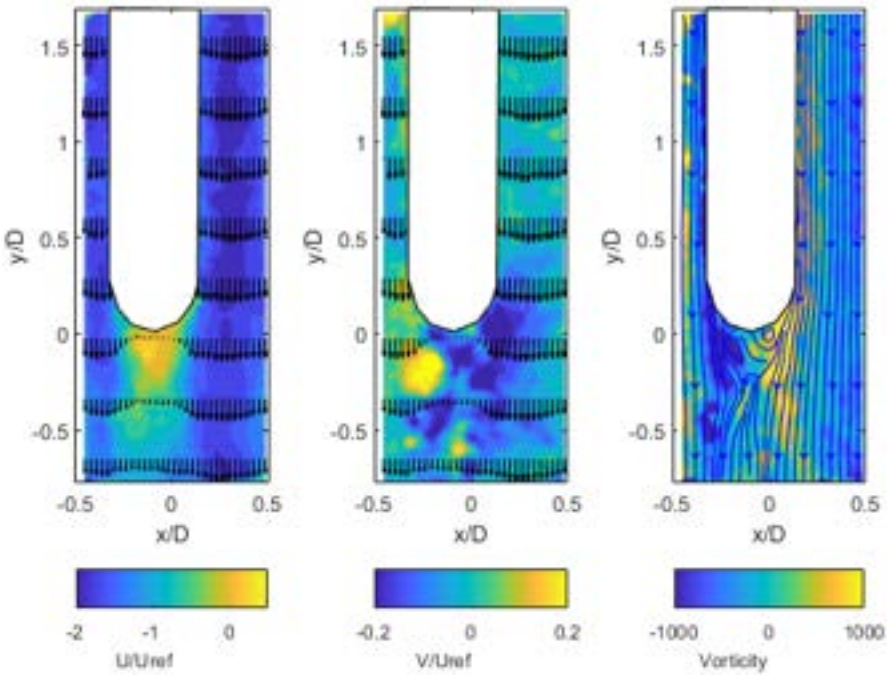

Figure 23: contours of axial and radial velocities with vector fields as well as vorticity and streamlines for the instantaneous vector field of the down-flow encountering the rod at the extreme left for a Reynolds number of 56k.

6. Brief Summary of Outcomes

This document provided a description of the single-phase cantilever rod experimental setup and of the conducted measurements. This information can be used to define the single-phase cantilever rod setup within numerical simulation models. The main outcomes are as follows:

- *An experimental setup has been developed to generate high-resolution benchmark data that exposes new physical insights for axial-flow-induced vibration of a rod in a confining tube, including both structural response and flow field measurements*
- *Interesting dynamics have been identified using the tracking experiments with clear differences between the free-clamped and clamped-free configurations*
- *PIV measurements (via both instantaneous and time-averaged measurements) provided clear characterisation of the flow field in the region near the rod tip (and at 10D below it) allowing these data to inform the development/validation of numerical models*

7. Data Requested

This document, hopefully, has provided a good insight into what has been investigated experimentally for the single-phase cantilever rod experiment and benchmark setup, in particular, rod motion and flow fields as function of applied flow rate, i.e., Reynolds number, so that the participants of the Benchmark 1 could get a better idea about simulation cases they would like to / can perform within this benchmark.

The evolution of the RMS displacement amplitudes from both front and side views of the rod motion as a function of the annulus Reynolds number was presented for both free-clamped and clamped-free vibrations. These results show that the rod vibration amplitude is generally higher for the case with flow directed downwards (clamped-free configuration). In this case the rod approaches the pipe wall and continues to exhibit high-amplitude dynamic motions from flow rates corresponding to annulus Reynolds number values >40,000. In the case with the flow directed upwards the rod vibrates as far as the pipe wall at high enough Reynolds numbers. At this condition the rod remains deflected in contact with the pipe wall, animated by a small-amplitude random vibration as it slides along the confining pipe wall. At lower flow rates the displacement of the rod is quite small and hence uncertainty can become large. Therefore, it may be argued that the flow rate corresponding to an annulus Reynolds number~15,000-20,000 is recognized as a reasonable lower limit for further numerical analysis. In addition to rod displacements and frequencies, also the preliminary results from PIV measurements for various mean flow variables have been presented.

All (new) measurements up to now have been performed with a rounded rod edge, and are shown in Figure 24 in comparison to the previous measurements within the VIKING project based on previously published results by Cioncolini et al. (2018). This comparison shows satisfactory repeatability of the experimental results and demonstrates the much wider range of measurements.

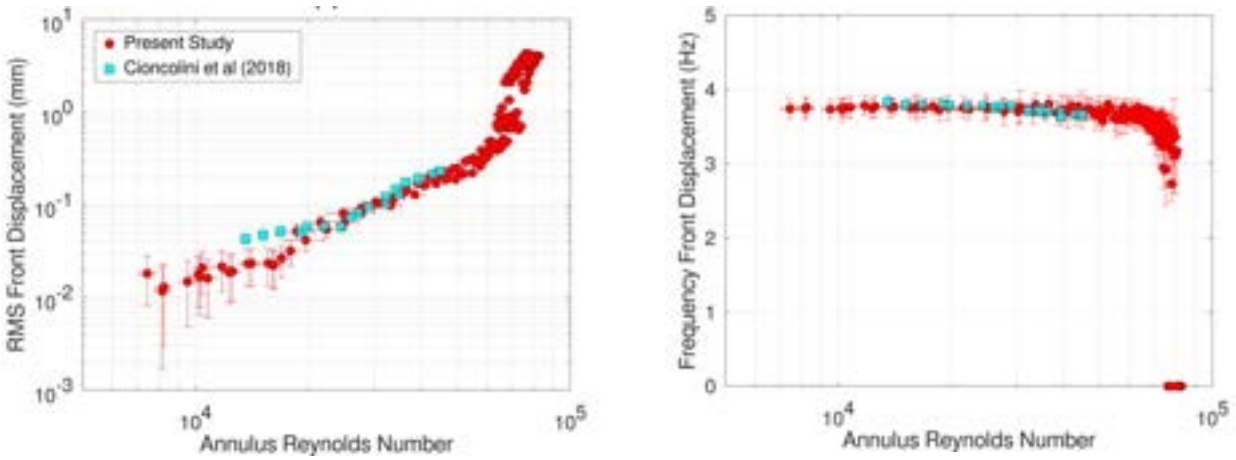

Figure 24: Comparison between present and previous data from Cioncolini et al. (2018).

The fluid flow data available from PIV measurements are sufficient for determining simulation inlet conditions. The presence of fully developed flow can be verified by the experimental results provided in the region below the rod free end. In fact, the flow straightener is considered to be located far enough below the rod tip so that a fully developed flow can be assumed upstream the rod free tip.

All main data are provided in this document. These data will also be provided in the journal publication that is currently being finalized for submission within the first quarter of 2023. Due to the chaotic component of the rod excitation (from turbulent buffeting), it is evident that it is not possible to exactly replicate any of the recorded time-series, which are therefore not provided. Numerical simulations should be run for long enough to extract meaningful summarizing statistics for the rod displacements (RMS, power spectra and dominant vibration frequencies, autocorrelations,…) to compare with the present data.

8. Appendix A

Figure 25 provides a more detailed illustration of the fixed-end connection of the rod within the test piece. In addition to the union cross connection, there are two reducers that slide one inside the other, and the rod is fixed in the top one.

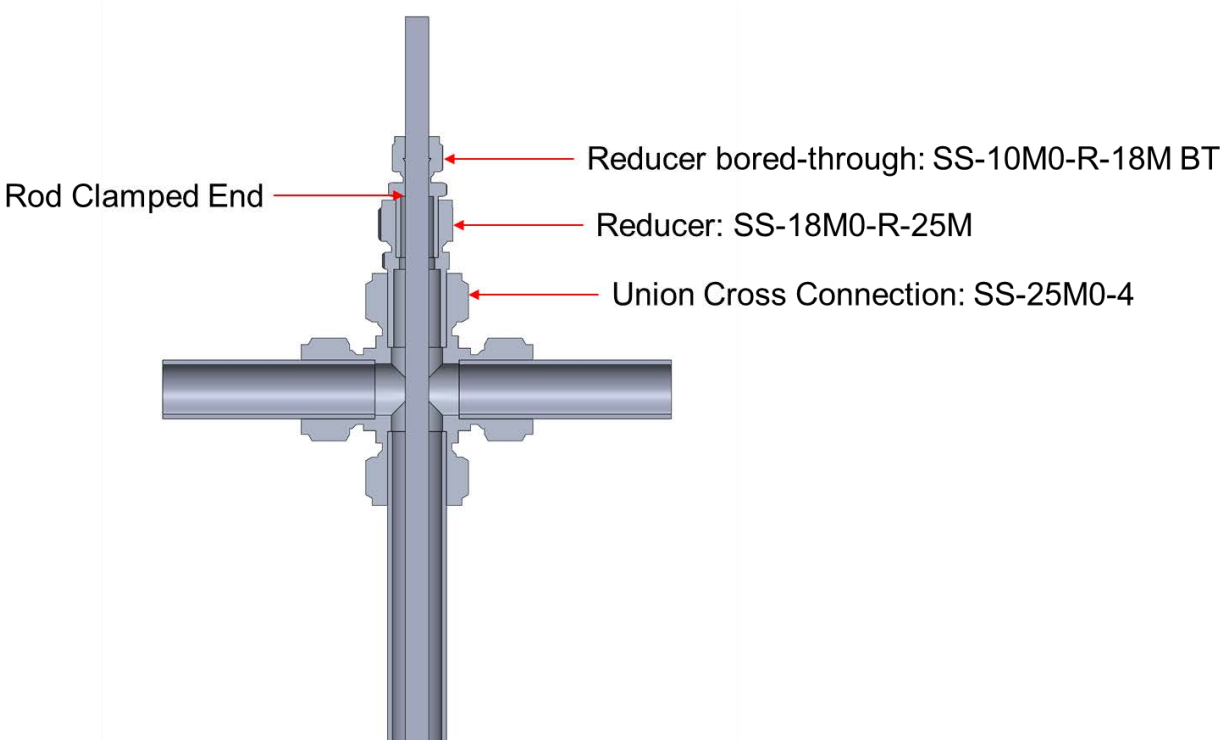

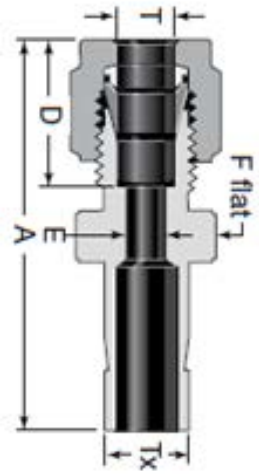

SS-10M0-R-18M BT (note that this reducer is bored-through so that the dimension E=T, so the CAD illustration above is a modified version of the diagram on the left obtained from the manufacturer's catalogue):

http://swagelok.thomasnet-navigator.com/item/category-2555/category-2348/ss-10m0-r-18m

SS-18M0-R-25M:
http://swagelok.thomasnet-navigator.com/item/category-2555/category-2348/ss-18m0-r-25m
SS-25M0-4:
http://swagelok.thomasnet-navigator.com/item/cross-connects-tubing-to-tubing/category-2326/ss-25m0-4

Figure 25: Illustration of the rod fixed end boundary condition.

9. Appendix B

Figure 26 provides some extra results from testing within air. These tests were conducted before starting the experimental campaign with water.

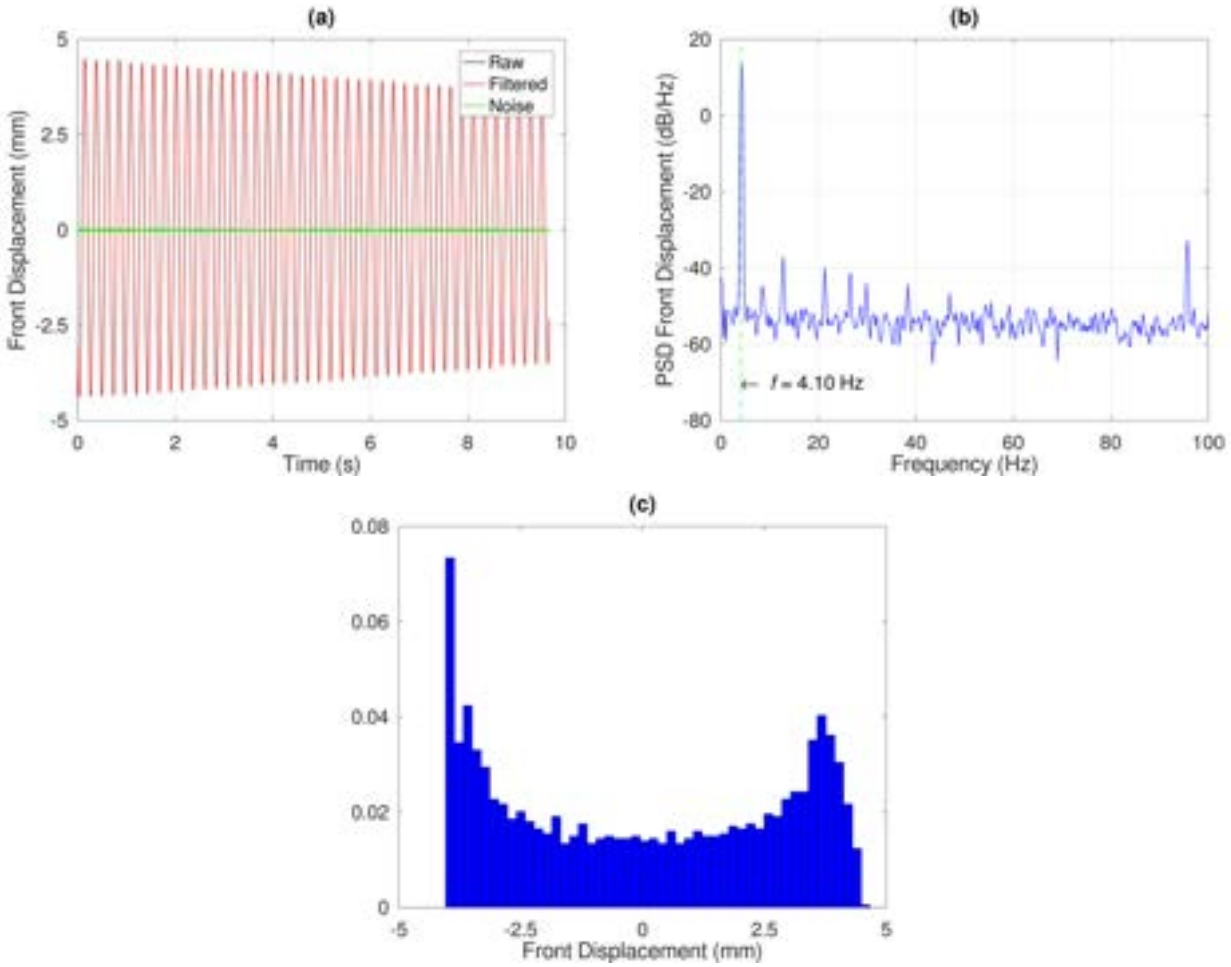

Figure 26: Free vibration in air: only front displacement was recorded; 200 fps recording frequency. Euler-Bernoulli mode-1 vibration frequency is 4.10 Hz.

10. Appendix C

Abstract for journal paper on rod tip shape influence:

The influence of tip shape on flow-induced vibration of a cantilever rod subject to axial water flow is experimentally investigated, through optical tracking of the rod movement and mapping of the instantaneous flow field around the rod tip. The experimental setup consists of a vertical cantilever rod housed within a tube. The rod tip shapes considered in this study include a blunt tip and cones with height-to-diameter ratios of 0.5, 1, and 2. The experiments were conducted across a Reynolds number range of 20k to 100k in both clamped-free and free-clamped configurations, representing opposite flow directions. The rod tip motion was

captured using fast video image tracking, whereas the flow field near the rod tip was obtained using particle image velocimetry (PIV). The rod vibration dynamics exhibited a primarily fuzzy period-1 behavior, characterized by a periodic motion with a chaotic component. Flutter-like oscillation and buckling were also observed at higher Reynolds numbers, depending on the flow direction. The mechanisms of fluid-structure interaction involved turbulent buffeting and movement-induced excitations. Unsteady flow separation around the rod tip was identified as a further contributing mechanism to flow excitation. In the clamped-free configuration, unsteady flow separation was more pronounced for the cone tips due to the increased rod surface area in the wake region, leading to larger vibration amplitude. In the free-clamped configuration, flow separation effects were more prominent for the blunt tip, as the streamlined cone shapes were less prone to flow separations. Overall, the rod with a blunt tip resulted in smaller displacement in the clamped-free configuration, while the rods with cone tips led to smaller displacement in the free-clamped configuration.

Full manuscript attached at end of this document.

Bibliography

Cioncolini, A., Silva-Leon, J., Cooper, D., Quinn, M. K., & Iacovides, H. (2018). Axial-flow-induced vibration experiments on cantilevered rods for nuclear reactor applications. *Nuclear Engineering and Design*, *338*, 102-118. (https://doi.org/10.1016/j.nucengdes.2018.08.010)

Eaton, J.W., Bateman, D., Hauberg, S., Wehbring, R. GNU Octave 4.2 Reference Manual 2017.

Smith, S.W., 2003. Digital Signal Processing, third ed, Newnes, Boston, USA.

Tip Shape Effects on the Axial-Flow-Induced Vibration of a Cantilever Rod

Hao Li[1,*], Andrea Cioncolini[2], Shanying Zhang[1], Hector Iacovides[1] and Mostafa R.A. Nabawy[1]

[1] School of Engineering, University of Manchester, Oxford Road, M13 9PL Manchester, UK

[2] Department of Mechanical Engineering (Robotics), Guangdong Technion - Israel Institute of Technology (GTIIT), 241 Daxue Road, Shantou, Guangdong, China, 515063

* Correspondence: hao.li@manchester.ac.uk

Email addresses: andrea.cioncolini@gtiit.edu.cn (AC); shanying.zhang@manchester.ac.uk (SZ); h.iacovides@manchester.ac.uk (HI); mostafa.ahmednabawy@manchester.ac.uk (MN)

Abstract

The influence of tip shape on flow-induced vibration of a cantilever rod subject to axial water flow is experimentally investigated, through optical tracking of the rod movement and mapping of the instantaneous flow field around the rod tip. The experimental setup consists of a vertical cantilever rod housed within a tube. The rod tip shapes considered in this study include a blunt tip and cones with height-to-diameter ratios of 0.5, 1, and 2. The experiments were conducted across a Reynolds number range of 20k to 100k in both clamped-free and free-clamped configurations, representing opposite flow directions. The rod tip motion was captured using fast video image tracking, whereas the flow field near the rod tip was obtained using particle image velocimetry (PIV). The rod vibration dynamics exhibited a primarily fuzzy period-1 behavior, characterized by a periodic motion with a chaotic component. Flutter-like oscillation and buckling were also observed at higher Reynolds numbers, depending on the flow direction. The mechanisms of fluid-structure interaction involved turbulent buffeting and movement-induced excitations. Unsteady flow separation around the rod tip was identified as a further contributing mechanism to flow excitation. In the clamped-free configuration, unsteady flow separation was more pronounced for the cone tips due to the increased rod surface area in the wake region, leading to larger vibration amplitude. In the free-clamped configuration, flow separation effects were more prominent for the blunt tip, as the streamlined cone shapes were less prone to flow separations. Overall, the rod with a blunt tip resulted in smaller displacement in the clamped-free configuration, while the rods with cone tips led to smaller displacement in the free-clamped configuration.

Keywords: Fluid-structure interaction; Tip shape effect; Nuclear reactor fuel rod; Fretting wear; Particle image velocimetry (PIV); Optical tracking

1. Introduction

The study of the vibration of slender cylindrical structures subjected to axial flow has attracted significant research interest in recent decades. This interest stems from the ever increasing importance of fluid-structure interaction phenomena observed in various scenarios, such as the anguilliform swimming of slender fish [1], suspension of cable-stayed bridges [2], and electrical power transmission lines. Moreover, axial-flow-induced vibration (axial-FIV) is of great importance in practical engineering applications, including heat exchangers, ocean mining [3], oil exploration [4], energy harvesting devices [5], and nuclear power plants [6–9]. In particular, within pressurized water nuclear reactor (PWR) cores, where the primary coolant flows axially through the gaps between adjacent fuel rods, axial-FIV becomes a critical concern. It can lead to fretting or intermittent contact between the fuel rods and their supports, resulting in long-term damage such as fretting wear and mechanical fatigue. Notably, fretting wear caused by FIV of nuclear fuel rods has been identified as a major contributor to fuel failure in PWRs [10,11]. Therefore, understanding the physical mechanisms governing such fluid-structure interaction, particularly in the case of slender structures in axial confined flows, is crucial for prolonging the lifespan of nuclear components.

The FIV problem in PWRs predominantly involves cantilever rods subject to nominally axial flow. In such systems, a primary source of disturbance arises from random pressure fluctuations within the turbulent boundary layer along the rod's surface [12]. These fluctuations create an unsteady transverse force that primarily affects the rod at its fundamental natural frequency. The resulting displacements remain relatively small due to the limited force amplitudes [13]. As the displacement of the rod accumulates, especially with an increase in flow rate, fluid forces stemming from transverse flow velocity towards the rod's surface introduce additional excitations to the rod vibrations. The mechanism involved is referred to as movement-induced excitation [7,8]. Furthermore, when the flow traverses the free end of the cantilevered rod, where geometric discontinuities are present, flow separation and vortex shedding can occur. These dynamic phenomena can significantly contribute to rod vibrations, providing excitations in close proximity to the rod's free end. Consequently, geometric variations at the rod free end is expected to substantially affect its vibration dynamics.

To date, limited studies have focused on the influence of the tip shape of the cantilever rod on its axial-FIV characteristics. Among these studies, Païdoussis [14] conducted an experimental

investigation into the dynamics of a cantilever rod featuring various end-piece configurations. The study focused on examining how the tapering of these end-pieces influenced the critical flow velocities associated with the buckling and oscillatory instabilities of the rod. The results showed that increasing the tapering of the end-pieces led to a reduction in critical flow velocities. Wambsganss and Jendrzejczyk [15] investigated vibration amplitude and damping characteristics for a clamped-free rod, i.e., flow moves away from the rod free-end, with various end shapes under nominally axial flow. They found that the amplitude of rod vibrations can vary by a factor of 4.5 when different end shapes are utilized. Rinaldi and Païdoussis [16] studied the dynamics of flexible free-clamped rods (i.e., flow directed toward the rod free-end) made of silicone rubber, with blunt and semi-spherical end-piece shapes. Experimental measurements revealed minor differences in the dynamic behaviour between the tip shapes. The rods initially exhibited small-amplitude flutter-like oscillations at low flow velocities, transitioning to static divergence at high flow velocities, accompanied by a decrease of vibration frequency. In the experiments of Cioncolini et al. [7], vibrations of free-clamped rods with blunt and semi-spherical tip shapes in axial water flow were measured in a range of Reynolds number between 13k and 45k. The study also involved measuring the flow field near the rod's free end using particle image velocimetry. The rod vibration dynamics observed in the experiments were qualitatively similar to those reported by Rinaldi and Païdoussis [16]. Their results also indicated that rods with blunt tip shapes exhibited larger vibration amplitudes than those with semi-spherical tip shapes, particularly at relatively high flow velocities, where movement-induced excitations significantly affected the rod vibration dynamics.

Currently, there is a notable limitation in comprehending the impact of tip shape on the vibration dynamics of a cantilever rod experiencing axial-FIV. The existing literature on this subject, as reviewed, is notably scarce. Furthermore, there lacks a convenient explanation for the fundamental mechanisms associated with the tip shape effects on axial-FIV of cantilever rods. This limitation can be attributed to two primary factors: firstly, prior research has primarily focused on the vibration dynamics of the rod itself, while neglecting the fluid dynamics near the rod free end, where abrupt geometric changes occur. Secondly, the range of tip shapes investigated has either been limited or lacks consistent variation, thereby failing to provide a comprehensive foundation for exploration. This gap in understanding persists, despite the fact that the flow patterns near the rod free end exert a critical influence on the rod vibration dynamics. As such, the current study aims to provide an improved understanding of the tip shape effects on axial-FIV of cantilever rods through comprehensive experiments involving both rod vibration and flow visualization measurements. The rod vibrations are measured using an optical tracking technique and the flow fields near the rod free end are mapped using particle image velocimetry (PIV). The present results can directly inform the design of nuclear

fuel rods, with a view at reducing their susceptibility to axial-FIVs. In addition, the complete dataset provided herein will prove instrumental in perfecting numerical methodologies for axial-FIV, whose development is hampered by the scarcity of high-resolution validation data [9,17–24].

The rest of this paper is organised as follows: the experimental setup and measurement methods are presented in Section 2. Rod vibration dynamics and flow field results for different tip shapes, including discussions on fluid-structure interaction mechanisms are presented in Section 3. Finally, the conclusions of this study are presented in Section 4.

2. Methods

2.1 Experimental Setup

2.1.1. Flow loop and test section

The experimental setup utilized in the present study follows the same configuration as in our previous work [8]. A schematic diagram of the flow loop is depicted in Figure 1. The test section is connected to a recirculating open loop system that is driven by a centrifugal pump (10HP Leeson pump). The temperature is measured using a direct immersion digital thermometer (ETI-Electronic Temperature Measurements Ltd) with a temperature range of 248-343 K, and accuracy of ± 1 K. The density and viscosity of the water are determined based on its temperature using NIST REFPROP [25]. To measure the mass flow rate, a turbine flow meter (Cole-Parmer) is installed downstream of the pump and upstream of the test section. The flow rate range of the turbine flow meter is 37.8-378 L/min, with an accuracy of ± 3.78 L/min.

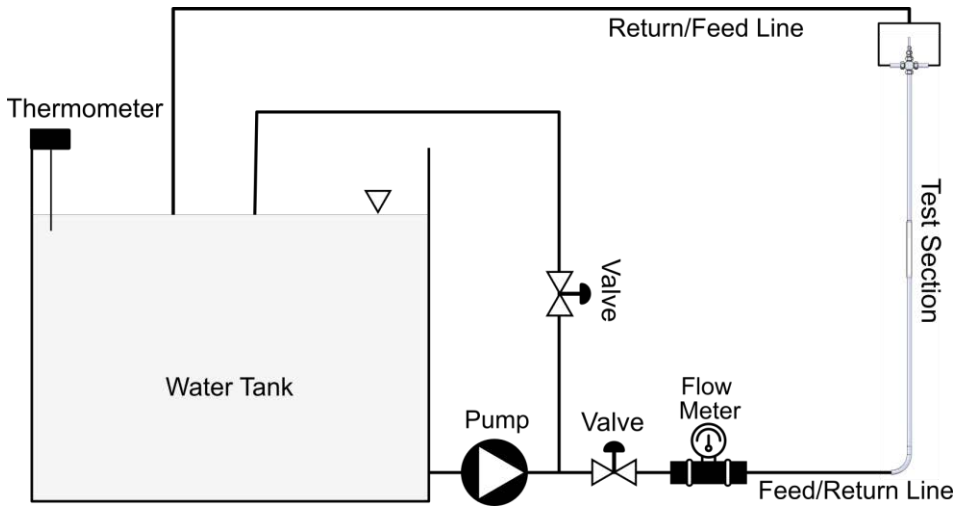

Figure 1. Schematic diagram of the experimental flow loop.

In Figure 2, a schematic of the test section is provided. The test section consists of a vertical cantilever rod that is confined within a tube. The rod is clamped at the top inside a union cross, while the bottom tip remains free. The flow can enter the test section from either the top or the bottom, and this is realized by switching the feed and return lines as shown in Figure 1. When the flow enters from below, it moves upwards, impinging on the free end of the rod, and then travels along the annular section towards the fixed end. This configuration is typically referred to as the "free-clamped configuration". On the other hand, when the flow enters from the top and moves downwards along the annular section, it passes the free end of the rod and exits from the bottom end of the confining pipe. This configuration is known as the "clamped-free configuration".

The confining tube used in the experiment has an inner diameter, D_{tube}, of 20.86±0.05 mm and an outer diameter of 25.06±0.01 mm. It is made of AISI 316 stainless steel and is firmly connected to a fixed frame that is attached to the experimental rig. To facilitate the optical detection of the rod motion and flow visualization measurements, a transparent Perspex section with a matching diameter was inserted near the tip of the rod. Due to the cylindrical shape of the confining pipe, an additional rectangular box with flat faces was attached around the transparent part of the test section to eliminate optical distortion via index matching. This surrounding structure, made of Perspex, has a square cross-section (this box section will be apparent later in Figure 4). During the experiments, the box structure was filled with water, which effectively eliminated any lensing effect and allowed for clear visualization of the flow through the cylindrical pipe.

At the bottom of the confining tube, a flow straightener is installed to eliminate swirl and secondary flows upstream of the rod in the free-clamped configuration. The flow straightener consists of three mildly squashed pipes, each with an inner diameter of 8.83 ± 0.05 mm and an outer diameter of 10.01 ± 0.06 mm. These pipes are 100 mm in length and are inserted into the confining tube at the bottom of the test section. On the other hand, at the top of the test section, a union cross (Swagelok SS-25M0-4) is used to connect the test section to two symmetrically routed pipes. This union cross also serves to hold the vibrating rod in place and ensure the fixed boundary condition. Note that, the use of a symmetric two-pipe configuration is implemented to avoid any localized crossflow near the fixed end of the rod, which could potentially affect the rod dynamics. The two symmetrically routed pipes connected to the branches of the union cross have the same inner/outer diameter as the confining tube of the test section.

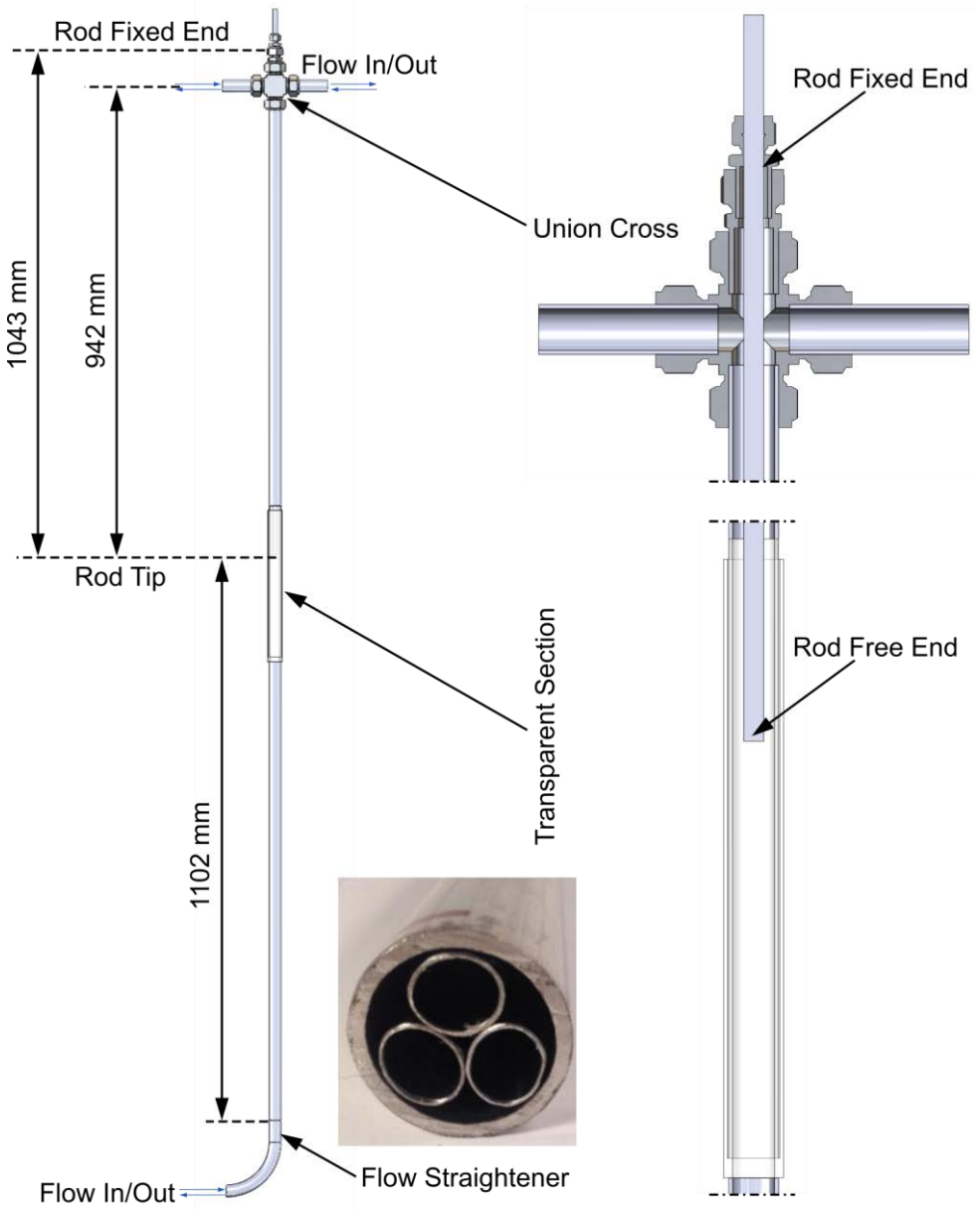

Figure 2. Schematic of the test section. The inserted figure shows the internal structure of the flow straightener. Rod and tube lengths for the blunt end rod are provided.

In the free-clamped configuration, the flow recovery distance extends from the top of the flow straightener to the free end of the vibrating rod, measuring 1102 mm for the blunt tip rod. This dimension decreases to 1082 mm when employing the cone tip shape with the largest height-to-diameter ratio (dimension of different tip shapes are provided in Figure 3). The flow recovery distance corresponds to approximately 50 times the diameter of the confining pipe. Our prior investigation [8] established that the flow straightener setup and flow recovery length were adequate for achieving fully-developed flow conditions upstream of the vibrating rod. On the other hand, in the clamped-free configuration, the upstream disturbances have relatively little

influence when the two incoming streams merge at the union cross. Therefore, no flow straightener was installed in the feeding pipes for this configuration.

2.1.2. Cantilever rod and tip shapes

The cantilever rod utilized in the study consists of an AISI 316 stainless steel circular tube with a density of 7990 kg/m³ and a Young's modulus of 193 GPa. The tube has an inner diameter of 8.83±0.05 mm and an outer diameter, D_{rod}, of 10.01±0.06 mm. The hydraulic diameter, D_{hyd}, defined as the annular gap between the confining tube and the rod, $D_{hyd} = D_{tube} - D_{rod}$, is therefore 10.85 mm. The Reynolds number is defined using the hydraulic diameter and mean flow velocity within the annular gap, $\bar{u}$, as:

$$Re = \frac{\rho \bar{u} D_{hyd}}{\mu}$$

where ρ is the density and μ the dynamic viscosity of water. Throughout the experiments, the water flow rate ranged from 0.57 to 2.68 kg/s, resulting in corresponding Reynolds numbers spanning approximately 20k to 100k. Notably, for nuclear reactor applications, the maximum Reynolds number achieved here is only one-fifth to one-sixth of the typical values encountered in nuclear reactor cores [8]. While it would be highly advantageous to align Reynolds numbers with reactor-prototypical conditions, the challenge lies in achieving optical access under high-pressure and high-temperature conditions. Despite these limitations, the present data retains its value for its contribution to the field.

In order to mimic the mechanical loading resulting from the fuel pellets in actual nuclear fuel pins, the present rod was filled with lead shot of loose texture. The lead shot has a density of 11.34 g/cm^3 and a diameter range of 0.3 to 1.6 mm. The lead shot densely filled the rod with a packing ratio of 84.6% to ensure even distribution and no motion inside the rod that would otherwise affect its vibrational dynamics. The measured linear mass density of the rod, accounting for both the rod material and the lead shot filling, is 588 g/m. It is worth noting that the lead shot filling clearly affects the mass density of the rod but has no influence on the flexural rigidity. This has been verified through an initial free vibration experiment conducted in our previous study [8].

The free tip shapes used in the current study include a blunt tip and cone tips with different height-to-diameter ratios (h/d). The schematics and dimensions of the end-pieces for different tip shapes are provided in Figure 3. To ensure that the end-pieces do not significantly affect the linear mass density of the vibrating rod, the blunt end-piece was made of lightweight aluminum with a density of 2.74 g/cm³ and has a mass of approximately 2.1 g. The different

cone end-pieces were 3D printed using hard resin. For each experimental run, these cone-shaped end-pieces were firmly affixed onto the flat surface of the blunt end-piece using a secure adhesive.

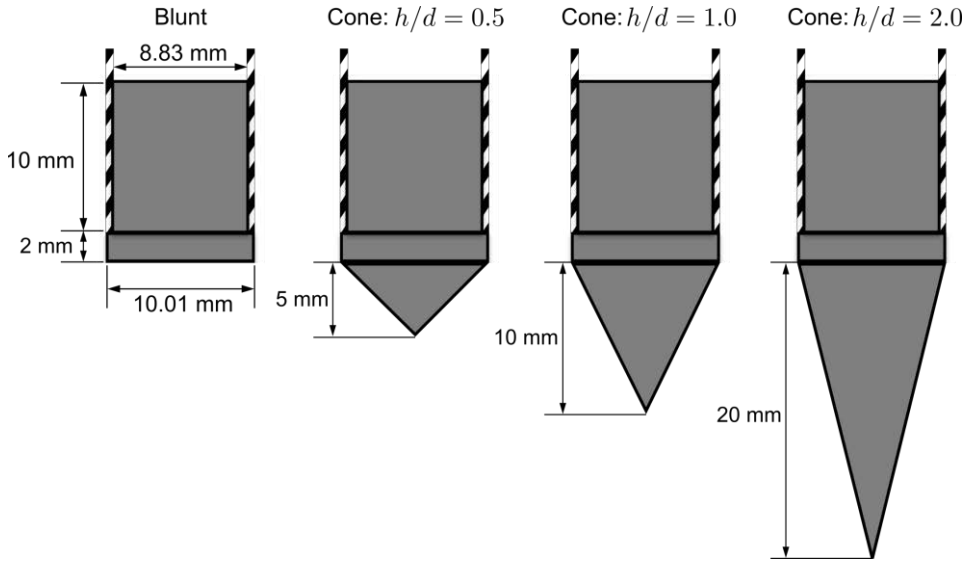

Figure 3. Schematic and dimension of end-pieces for cantilever rod.

2.2 Measurement Tools

2.2.1. Rod vibration measurement

The flow-induced motion of the rod tip was recorded using a high-speed imaging camera (Sony Alpha A6300). The recordings had an image resolution of 1280 x 720 at a frequency of 100 frames per second and lasted for a duration of 60 seconds. To capture both the front and side motions of the vibrating rod, a mirror was placed at a 45-degree angle on the side of the transparent section. A schematic illustrating this setup is provided in Figure 4.

The video image processing method for motion tracking utilized in this study builds upon the techniques developed by the group for axial-FIV and fluid structure interaction studies [26–30]. The recorded frames were first converted to grayscale, then binarized, and complemented to isolate a single feature corresponding to the vibrating rod tip. The position of the centroid of the rod tip was computed and recorded, enabling the assembly of the displacement time-series for both the front and side motions. Combining these time-series provided a characterization of the rod motion in 3D. The image processing and subsequent time-series analysis were all performed using the free software GNU Octave (version 4.2.2) [31]. The analysis relied solely on the built-in features provided by the 'image' and 'signal' packages within GNU Octave.

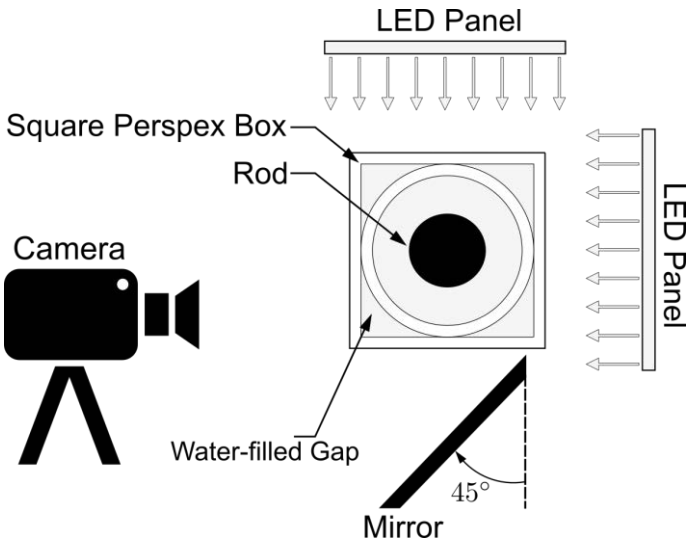

Figure 4. Schematic of rod vibration measurement setup.

In this study, we analysed the displacement time-series of the vibrating rod using a series of methods to fully expose the rod dynamic behaviour. Initially, root-mean-square (RMS) values were computed from the acquired displacement time-series data to quantify the overall magnitude of the rod's motion. Subsequently, the power spectrum, which reveals the frequency content of the motion, was computed using the Welch method [32]. To enhance the quality of the time-series data and reduce noise in the time domain, a 13-point Henderson moving-average filter was applied [33]. The filtered time-series data, after noise reduction, was then utilized for the remaining analyses, including the computation of the displacement histogram, the autocorrelation function, and reconstruction of the attractor in phase-space.

The error in the RMS displacement of the rod tip was determined through preliminary tests when the pump was switched off and the vibrating rod remained motionless in stagnant water. Fluctuations observed in the time series during these tests were utilized as an estimate of noise generated during image acquisition and analysis procedures. The experiments were repeated multiple times, yielding a measuring error of less than 10 μm. The primary frequency of the rod's vibration was determined by identifying the dominant peak in the power spectrum of the displacement time-series, and the corresponding measurement error was calculated as half of the full width at half maximum of this peak.

It is important to note that the experimental method for rod vibration measurement was validated through preliminary free vibration experiments in still water. During these preliminary tests, the test section was filled with static water, and the rod was manually displaced from equilibrium. The subsequent free vibration of the rod was recorded and analyzed. The

measured free vibration frequency and damping ratio of the rod align closely with theoretical predictions. Specifically, the experimentally determined free vibration frequency of the rod, 3.72 Hz, closely corresponds to the value estimated using Euler-Bernoulli beam theory. Additionally, the experimentally determined damping ratio of 0.015±0.001 closely matches the theoretical model proposed by Rogers et al. [34] for a vibrating rod in a fluid-filled annulus, with a deviation within 10%. For more details regarding the validation procedure and an extensive validation dataset, we direct readers to our previous study [8].

2.2.2. Flow field measurements

The flow field near the free end of the vibrating rod was investigated using the Particle Image Velocimetry (PIV) technique. PIV measurements were conducted subsequent to the acquisition and analysis of rod displacement data. These measurements were performed at typical Reynolds numbers of 25k and 83k, specifically selected to provide a comprehensive characterization of the flow field surrounding the vibrating rod tip under both low and high flow rate conditions.

A schematic of the PIV setup used in this work is shown in Figure 5. The measurements were performed using a Dantec Dynamics PIV system, which includes a double cavity Nd: YLF laser. The laser has a maximum output energy of 15 mJ and operates at a wavelength of 527 nm. The laser was connected to an articulated light arm equipped with a beam-width-control optic that includes a divergent lens. This allowed for the creation of a two-dimensional vertical laser sheet that spanned the center plane of the flow field. The thickness of the laser sheet was adjusted by varying the distance between the built-in lenses, and was set to approximately 1 mm. The laser sheet was oriented at an angle to the flow direction to capture the flow patterns near the rod tip. To ensure visibility of the flow field on the obscured side of the vibrating rod, a mirror was positioned beside the test section. This mirror reflected the laser sheet, illuminating the flow field from the opposite side of the rod, as illustrated in Figure 5a.

In the PIV measurements, we employed a high-speed camera (Phantom V310) fitted with a Nikon AF Micro 60 f/2.8D lens. The camera operated in double-frame mode at a frequency of 200 Hz, capturing images at a resolution of 1280 x 800 pixels. To facilitate flow visualization, hollow glass spheres (HGS-10) with a nominal diameter of 10 μm were introduced into the test water as seeding particles. The particle concentration was empirically adjusted to achieve the desired resolution. Prior to each experimental run, the rig was operated at its highest flow rate for several minutes to ensure the uniform dispersion of these particles.

The laser pulses were controlled using a Q-switch delay technique. The time delay between successive laser pulses was empirically adjusted based on the flow velocity of the specific

case under study, with shorter delay times for cases with higher flow velocities. Typically, a delay time of 20-50 μs was employed to achieve adequate particle displacement without the excessive loss of particles from the flow visualization region. For each case, the recorded images were carefully reviewed to ensure that they captured the rod while its centroid axis remained within the measurement plane. Following acquisition, the recorded images were processed using the PIVLab toolbox [35] to extract the flow field surrounding the vibrating rod tip.

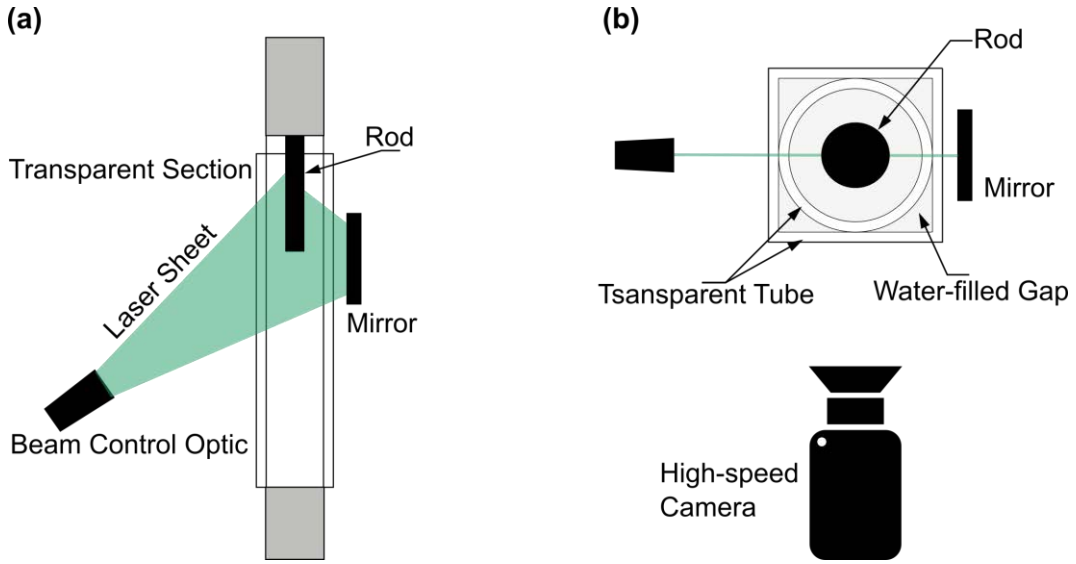

Figure 5. Schematics of the PIV set-up arrangement. (a) Front view, and (b) top view including high-speed camera.

3. Results and Discussion

3.1 Clamped-Free Configuration

3.1.1. Rod vibration dynamics

Figure 6 presents the results of the rod vibration for the clamped-free configuration, considering different tip shapes. The RMS displacements and vibration frequencies are plotted against the Reynolds number. The vibration frequencies correspond to the dominant peaks observed in the power-spectral-density (PSD) of the rod displacement time series, which is exemplified in the Appendix A for typical Reynolds numbers. Figure 7 further presents the tip trajectory of the rod, including 3D space-time illustration and 2D polar trajectory map at two typical Reynolds numbers. Note that, the wall limit horizontal line in Figure 6 represents the maximum distance the rod can achieve before hitting the confining tube wall, which is 5.4 mm

in this case. Additionally, a vertical line helps identify the lower limit of Reynolds number investigated.

Figure 6a shows the resultant radial RMS displacement of the rod. The results indicate that transitioning from a blunt tip to a cone tip with an increasing height-to-diameter ratio, generally results in increased vibration displacement. On the other hand, In Figure 6b, the front and side RMS displacements are presented separately. It can be observed that the responses and dynamics obtained from the front and side motions are similar, both qualitatively and quantitatively, where the vibration amplitudes and frequencies gradually increase as the Reynolds number increases for all tip shapes.

Two distinct variation trends of the radial displacement with respect to Reynolds number have been identified, depending on the tip shape. Starting with the rod with the blunt tip, on a log-log scale, the RMS displacement increases linearly with the flow Reynolds number, for the Re range tested (20k-100k). For the cases of cone tips with h/d = 0.5 and 1, there is also a monotonic increase in the RMS displacement with the flow Reynolds number, but with a progressive increase in the RMS values at each Reynolds number as the blunt tip is replaced by the cone of h/d = 0.5 and then by the cone of h/d = 1. Notably, the slope of increase of RMS radial displacement with Reynolds number is similar for the blunt tip rod and cone tip rods with h/d = 0.5 and 1. For the rod with the cone of h/d = 2, however, the vibration behaviour is radically different. At the low end of the Re range (~20k) the RMS displacement levels are lower than those of the rods with the three other tips, but the slope of increase with Reynolds number is much higher. A transition in rod vibration dynamics is evident at a Reynolds number of 45k, marked by a noticeable increase in the steepness of the rod displacement slope. As a result of this steeper rise of RMS displacement, for Reynolds number levels beyond 50k, the rod hits the confining wall of the tube, causing the displacement to plateau. It is worth noting that for all other tip shapes, the rod does not hit the confining tube, even at the highest Reynolds number tested, which is approximately 100k.

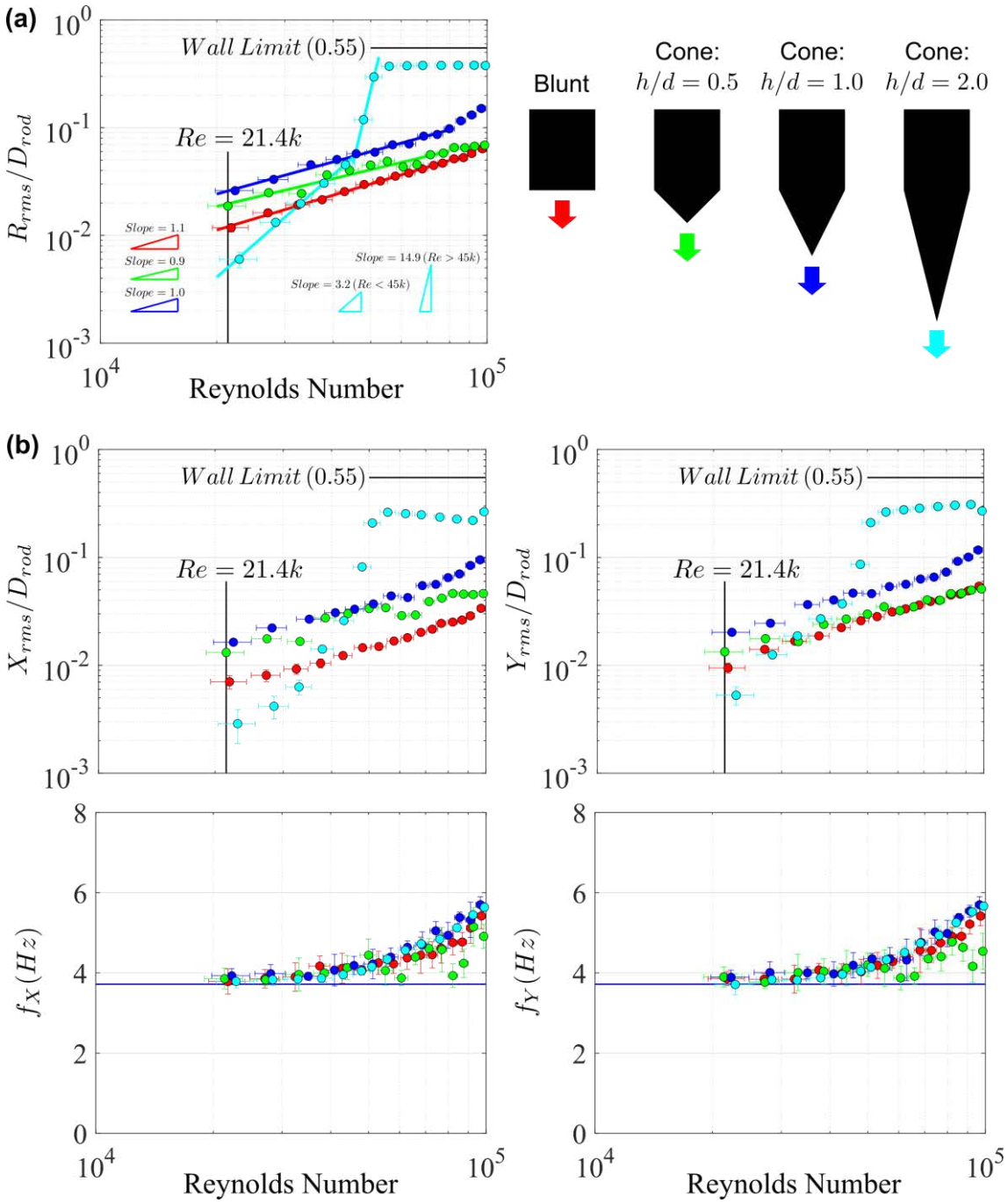

Figure 6. RMS displacement and frequency for rod with different tip shapes against Reynolds number for the clamped-free configuration. (a) Resultant radial displacement. (b) Displacements from the front, X, and side, Y directions. The displacement is scaled using the rod outer diameter (D_{rod} = 10.01 mm).

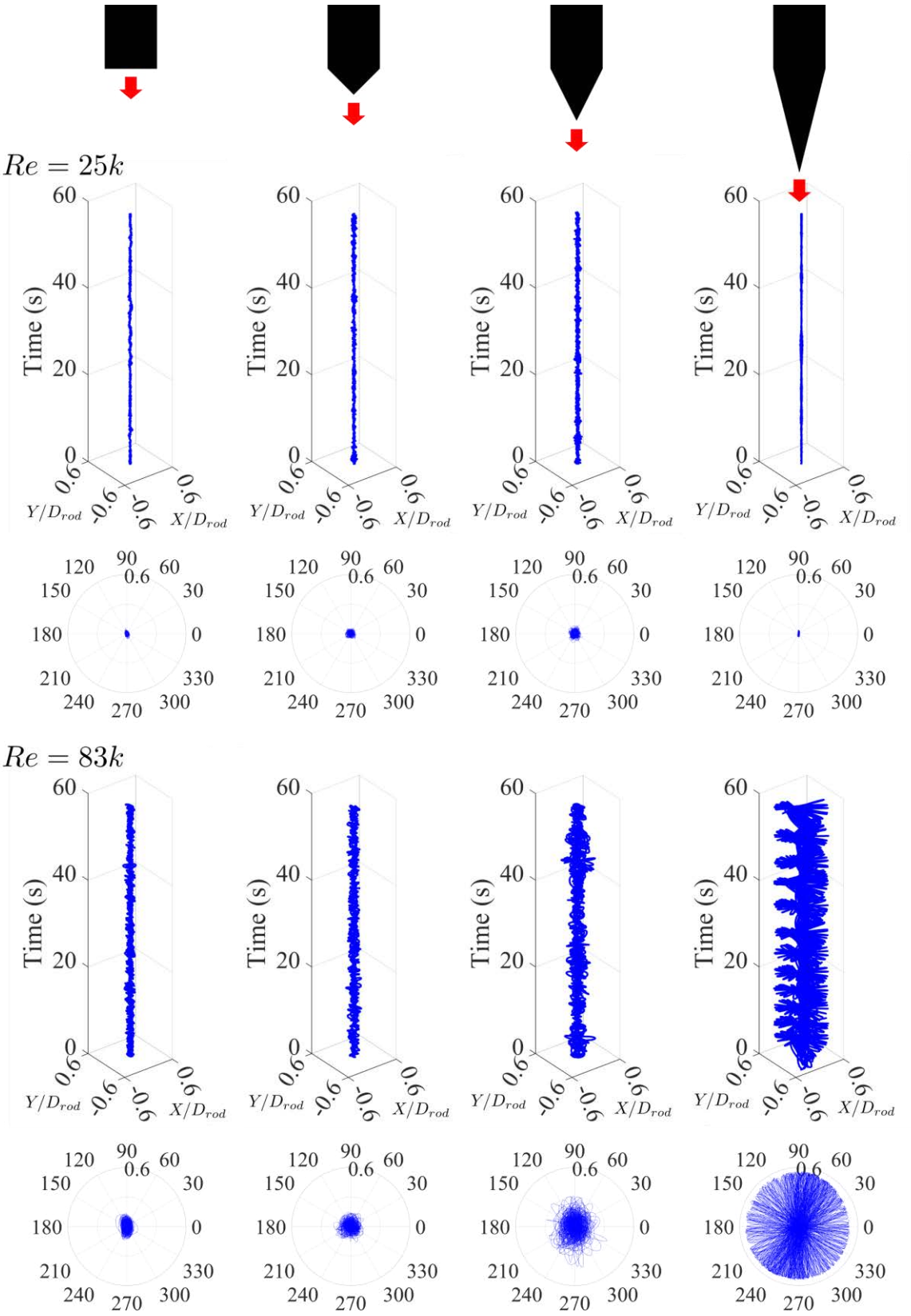

Figure 7. Displacement trajectory in 3D (space-time) and 2D (space only) for rod with different tip shapes at Reynolds number of 25k and 83k for the clamped-free configuration.

The results highlight clear differences in the dynamic behaviour of rods with different tip shapes. In particular, the dynamic behaviour of the blunt tip and cone tips with h/d = 0.5 and 1 exhibit similarities, contrasting with the cone tip with h/d = 2. To better clarify the vibrating rod dynamics, additional results for two typical Reynolds number values of 25k and 83k are provided in the Appendix A. These two Reynolds numbers presented exemplify both ends of the measured Reynolds number range. The results include: 1) a sample (5 s long) of the displacement time-series; 2) the normalized histograms; 3) the power spectrum; 4) the autocorrelation function; 5) the reconstructed attractor for phase-space topology. All results include both the front and side motions. Figures A1 – A4 encompasses the results for the clamped-free configuration. For all the tip shapes except the cone tip with h/d = 2, the displacement histograms are “bell-shaped”, the autocorrelation functions are periodic and fast-decaying, and the reconstructed attractors are “blob-like”, suggesting that the rod vibrations encompass both periodic and chaotic components, a dynamic response normally referred to as fuzzy period-1 motion [36]. For the cone tip with a h/d = 2, the dynamic behaviour is similarly fuzzy period-1 motion at the low Reynolds numbers. However, at the higher Reynolds number of 83k, the displacement histograms become wider and tend to have a "bridge-shaped" distribution. The decaying of the autocorrelation functions also become slower, indicating that the periodic component becomes more prominent compared to the chaotic component of the rod motion. Finally, the reconstructed attractors tend to be “ring-shaped”. These results indicates that the fuzzy period-1 motion observed at low Reynolds numbers evolves into a flutter-like large-amplitude oscillation at higher Reynolds number values.

3.1.2. Mechanism of FIV

Flow fields near the rod tip for the different tip shapes at two Reynolds numbers of 25k and 83k are visualized in Figures 8 and 9, respectively. Figure 8 illustrates instantaneous velocity magnitude fields, accompanied by quiver plots representing the velocity vectors. Complementing this, Figure 9 presents the vorticity fields and streamlines to provide a more comprehensive view of the flow characteristics.

In Figure 8, the wake regions are clearly depicted, showing velocity deficits downstream of the rod ends. As anticipated, the blunt tip rod exhibits the highest velocity deficit due to its blunt geometry. The wake velocity deficit region decreases for the cone tip shapes, and this reduction becomes more pronounced with an increase in the cone's height-to-diameter ratio. In cases where the rod is deflected, such as the cone tip with h/d = 2 at Reynolds number of 83k, the flow velocity is high in the side passage left behind the rod, while the wake is present on the other side where the rod is deflected.

In Figure 9, it can be observed that for the rod with a blunt tip shape and cones with h/d = 0.5 and 1, shear layers with high vorticity are present on both sides of the rod at both Reynolds numbers. These shear layers form due to the separation of the turbulent boundary layer from the edges as the flow passes through the geometric transition between the cylinder and the cones. Downstream of the rod tips, recirculating vortices are formed within the shear layers and subsequently shed into the wake. In contrast, for the cone tip with h/d = 2, no significant flow separation is observed in the case of the low Reynolds number (25k) and the flow field downstream of the tip looks streamlined and stable. When the Reynolds number rises to 83k, minor flow separation bubbles can be detected over the surface of the h/d = 2 cone, and more importantly, perhaps, the flow field downstream of the tip now appears to be unstable.

The above results suggest that turbulent buffeting and unsteady flow separation are two main sources of excitation for rod vibrations. Turbulent buffeting arises due to the presence of turbulent shear layers at the vicinity of the rod tips, whereas unsteady flow separation at the geometric transition of the rod tips, when present, provides an additional source of excitation to the rod vibration. Unsteady flow separation is evident, for the lower Reynolds number, at the cone tips with h/d = 0.5 and 1, and for the higher Reynolds number at the tips of all cone shapes. These observations provide a clear explanation for the different trends observed in rod vibration dynamics, as depicted in Figure 6. At low Reynolds numbers, unsteady flow separation has a dominant effect on rod vibrations for the blunt tip and cone tips with h/d = 0.5 and 1, whereas, for the cone tip with h/d = 2, turbulent buffeting is the primary source of excitation. This, at lower Reynolds numbers, results in a larger RMS displacement for the blunt tip and cone tips with h/d = 0.5 and 1. Notably, at higher Reynolds numbers, as the cone height-to-diameter ratio increases, the effect of unsteady flow separation is amplified due to the larger surface area available for flow excitations. This explains the observed increase in RMS displacement with cone height-to-diameter ratio at high Reynolds numbers.

As the Reynolds number increases, the displacement of the rod becomes larger, and movement-induced excitations gradually become the dominant influence on rod vibrations [8]. In this regime, the tip shape also plays a significant role in the fluid-structure interaction mechanism affecting the rod vibration dynamics. The key factor is once again flow detachment near the rod tips. In movement-induced excitations, the displacement of the rod leads to a fluid force response acting on the rod's surface. Due to the large ratio between the fluid and the structure velocities (the ratio between the mean fluid and structure velocities is above 300 for the investigated cases), the reaction fluid force is almost immediate [8]. Hence, the reaction fluid force provides an excitation at the same frequency as the natural frequency of rod vibrations, thereby significantly impacting the rod dynamic behavior. In an attached flow scenario, the displacement of the rod leads to a large fluid force response that follows a linear

relationship with respect to the rod displacement, whereas in a detached flow scenario, the boundary layer is unable to sustain the large pressure gradient along the rod's surface, resulting in a weaker fluid force response and energy losses into the wake vortices. Consequently, tip shapes that result in flow separation are less sensitive to movement-induced excitations.

The above reasoning explains the observed trends in rod vibration dynamics depicted in Figure 6. When comparing the cases of blunt tip shape with the cone tip shape with h/d = 2, the former exhibits a relatively small increment in displacement with increasing Reynolds number, showing an almost constant slope throughout the range of Reynolds numbers. In contrast, the latter demonstrates a rapid increase in vibration displacement as Reynolds number increases. Notably, for the cone tip with h/d = 2, the critical Reynolds number for the primary mechanism to switch from turbulent buffeting to movement-induced excitations occurs at 45k. At this Reynolds number, the rod RMS displacement rapidly escalates with the increase of Reynolds number, leading to a flutter-like oscillation and eventually hitting the confining tube wall. This transition is attributed to the accumulation of rod displacement, which is sufficient to induce substantial movement-induced vibrations at the Reynolds number of 45k.

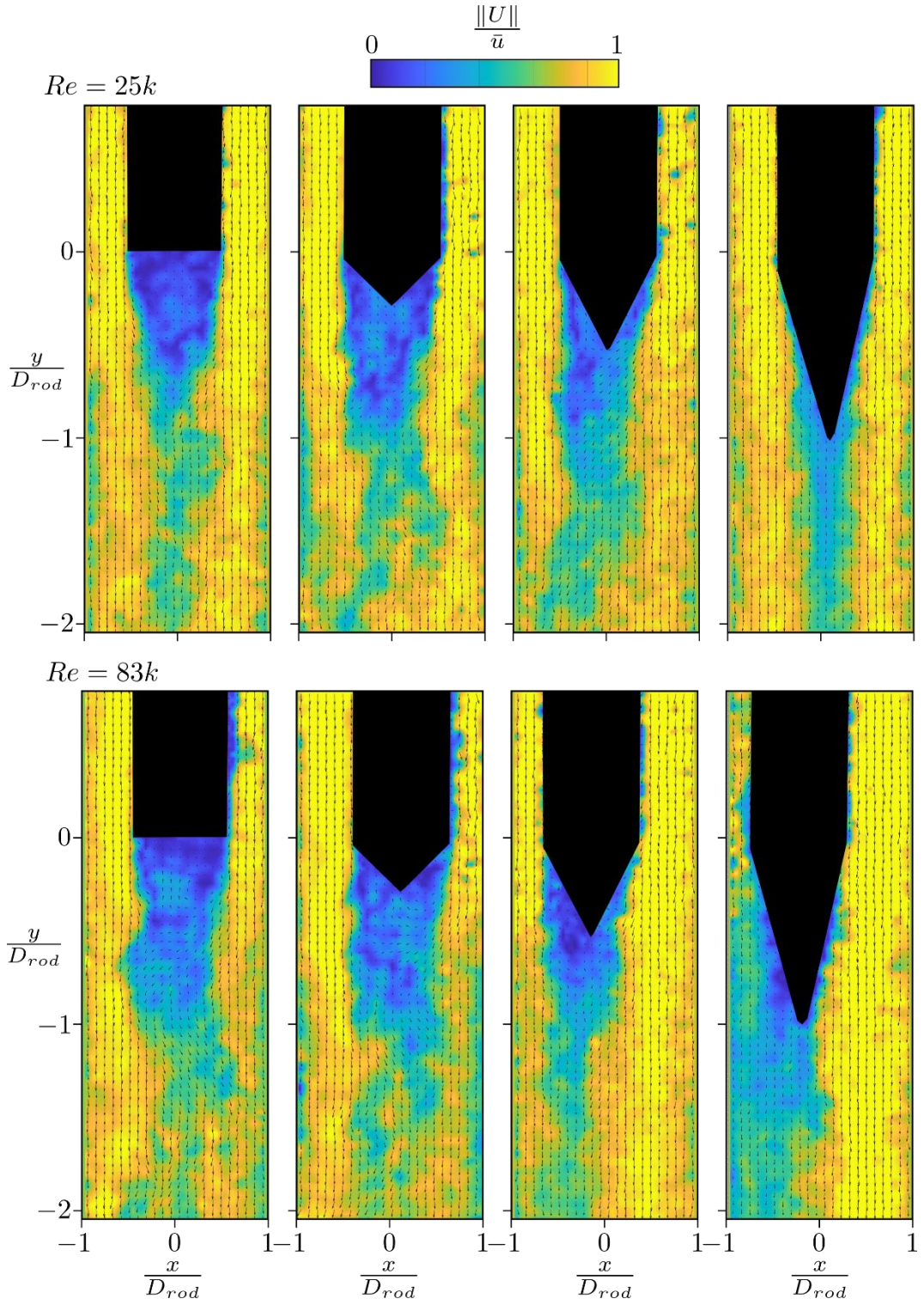

Figure 8. Velocity magnitude normalized with respect to the mean flow velocity within the annular gap, $\bar{u}$, for different tip shapes at Reynolds number of 25k and 83k. Quiver vectors indicate velocity field.

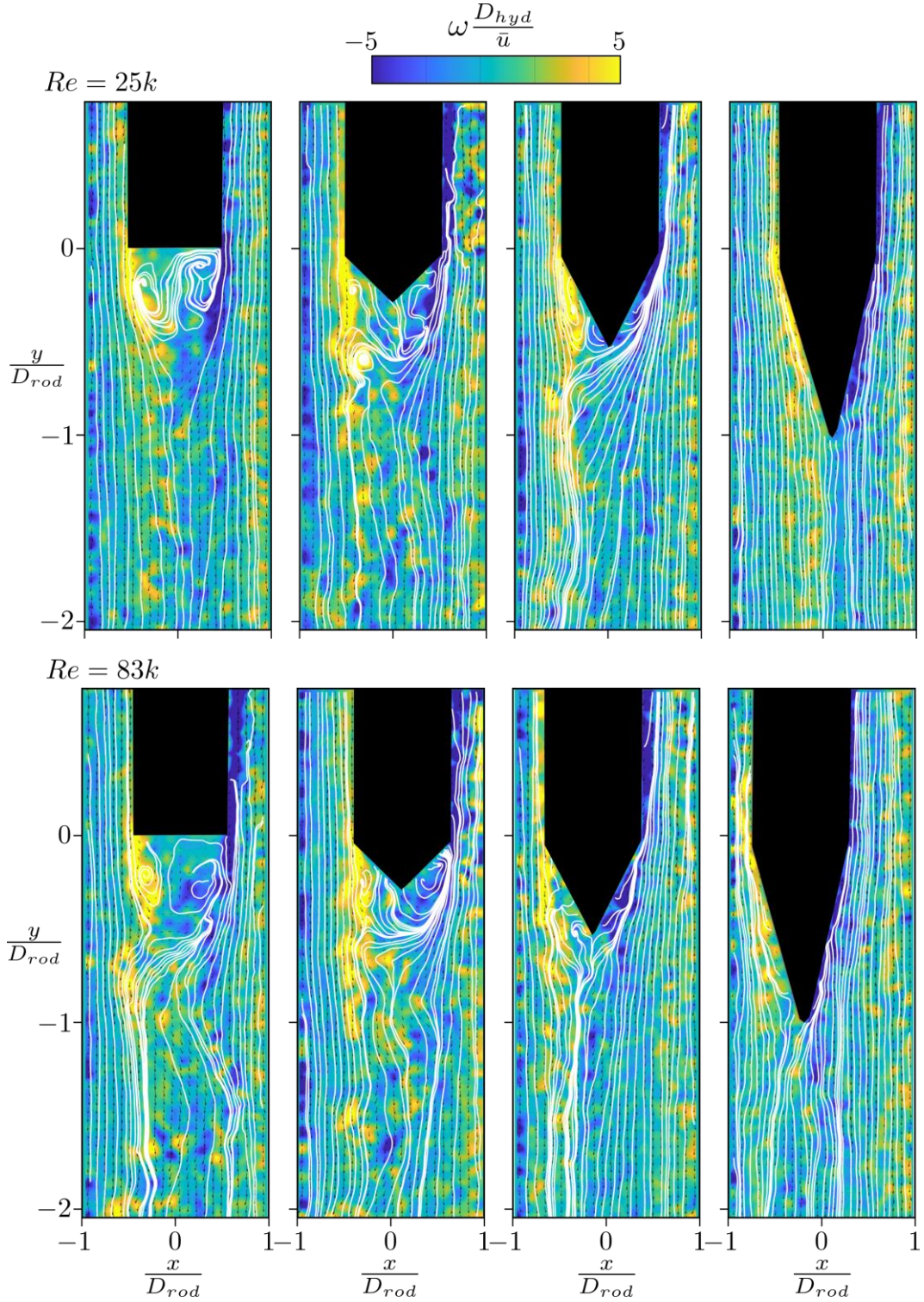

Figure 9. Vorticity and streamline for different tip shapes at Reynolds number of 25k and 83k. Vorticity, ω, is obtained by taking the curl of the velocity field.

3.2 Free-Clamped Configuration

3.2.1. Rod vibration dynamics

The results of the rod vibration displacements for the free-clamped configuration, considering different tip shapes are presented in Figure 10. Examples of the rod tip trajectory, including 3D space-time illustration and 2D polar trajectory map at two typical Reynolds numbers are presented in Figure 11. Regardless of the tip shape, the RMS displacements of the rods shows almost a linear increase with the increase in Reynolds number before buckling occurs, whereas the vibration frequencies decrease as the Reynolds number increases.

At high Reynolds numbers, buckling was observed in the cases of the blunt tip and cone tips with h/d = 0.5 and 1, but not for the cone tip with h/d = 2. Note that, when buckling occurs, the rod remains nearly still at the buckled position, attaching to the confining tube wall. As a result, the vibration frequency drops to zero, as illustrated in Figure 10b when the RMS displacement of the rods reaches the wall limit. The range of Reynolds numbers at which buckling occurs lies between 80k and 95k. However, it should be noted that the buckling Reynolds number is sensitive to the initial condition of the testing setup, and for example any minor misalignment of the rod can lead to a considerable change in the buckling Reynolds number (for the tests documented herein, the rod misalignment was within 10^{-3} radians, estimated by measuring the rod tip offset at zero flow rate condition). Finally, it is worth mentioning that hysteresis behaviour was observed for the buckled cases: when increasing the flow rate, the Reynolds number for the onset of buckling is higher than the Reynolds number at which the rod returns to a vibrational state as the flow rate decreases. This behaviour is consistent with our previously reported observations for a rod with a semi-spherical tip shape [8].

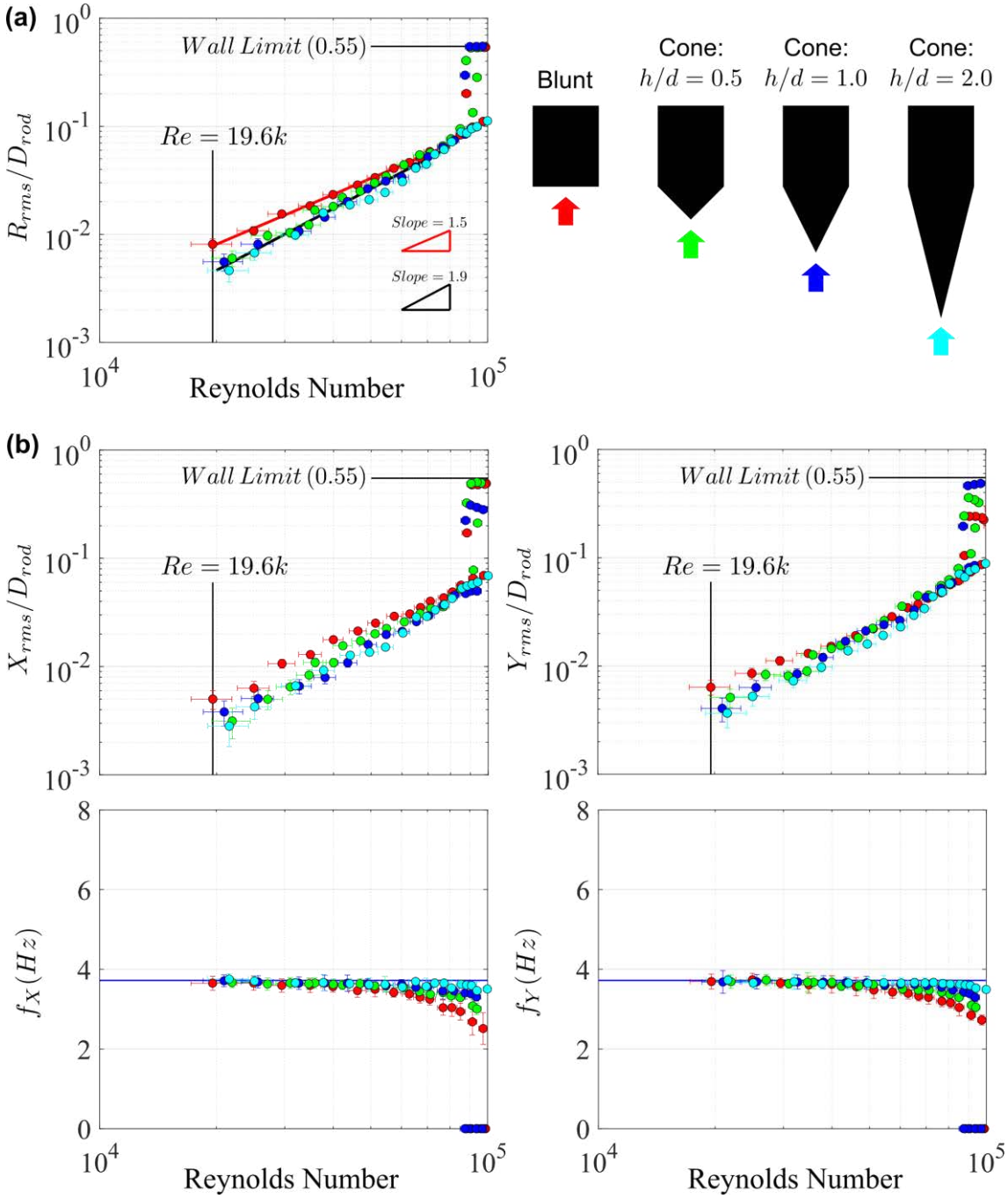

Figure 10. RMS displacement and frequency for rod with different tip shapes against Reynolds number for the free-clamped configuration. (a) Resultant radial displacement. (b) Displacement from the front, X, and side, Y directions. The displacement is scaled using the rod outer diameter (D_{rod} = 10.01 mm).

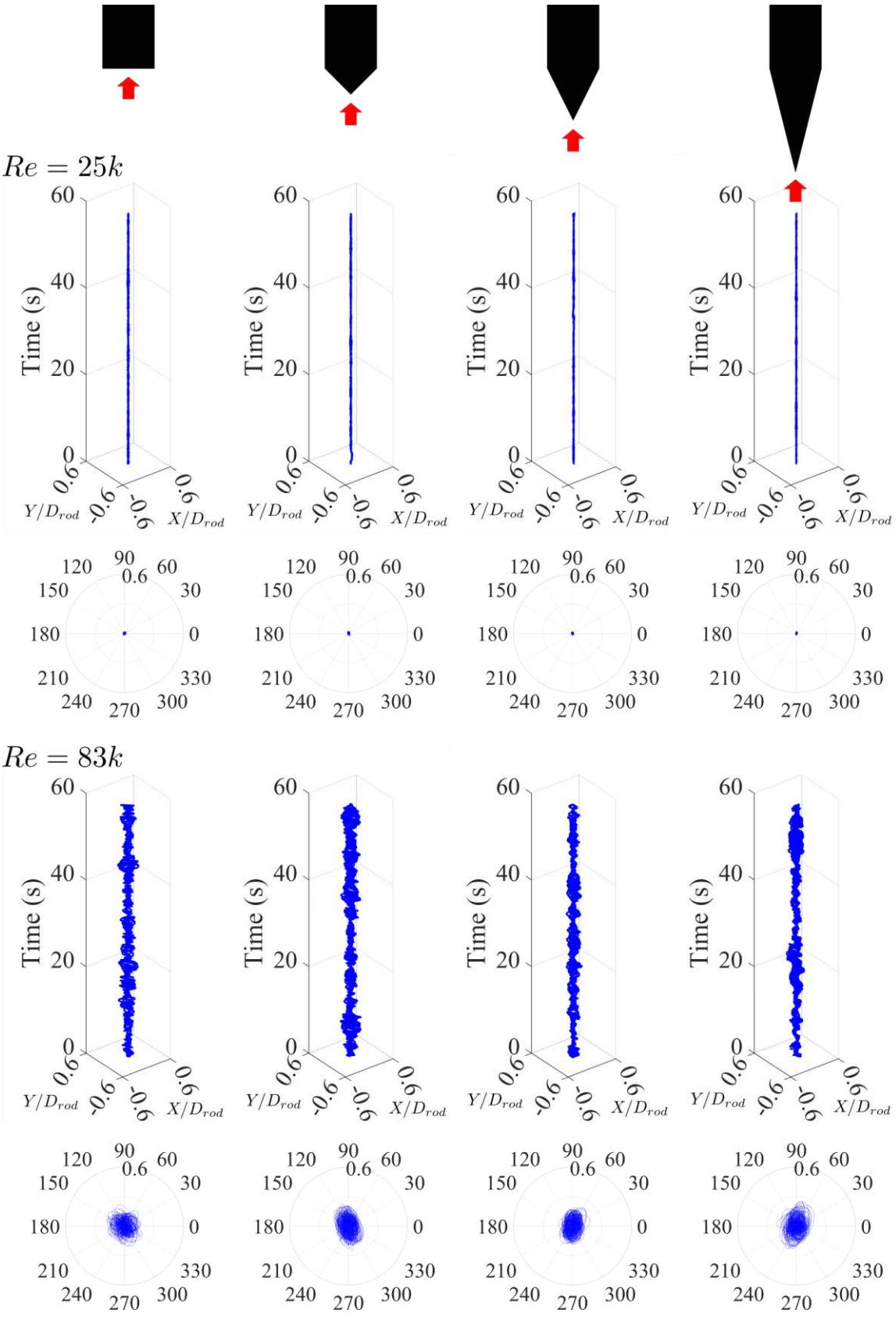

Figure 11. Displacement trajectory in 3D (space-time) and 2D (space only) for rod with different tip shapes at Reynolds number of 25k and 83k for the free-clamped configuration.

Examples of the rod vibration analysis results for different tip shapes at Reynolds numbers of 25k and 83k are illustrated in Figures A5 – A8. The histograms display a "bell-shaped" distribution, while the autocorrelation functions exhibit periodicity and fast decay. The reconstructed attractors are "blob-like". All these features indicate that the motion of the rods is fuzzy period-1. It is noteworthy that, as the Reynolds number increases, the periodic component of the rod vibration gains greater importance, resulting in a wider distribution of the displacement histogram and a slower decay in the autocorrelation function compared to lower Reynolds number cases. Throughout the experiments, no flutter-like oscillation was observed within the range of Reynolds numbers investigated. In the cases where buckling was observed, i.e., the blunt tip and cone tips with h/d = 0.5 and 1, the rod motion transitioned rapidly from fuzzy period-1 to buckling, within a narrow range of Reynolds numbers for the transition, and no intermittent motions were observed. Figure 10a also demonstrates that, prior to buckling, the blunt tip rod generally exhibits larger RMS displacement than the cone tip shapes at low Reynolds numbers. However, as the Reynolds number increases, the difference in RMS displacement between the blunt tip and the cones tends to diminish.

3.2.2. Mechanism of FIV

Examples of flow fields near the rod tip for different tip shapes at two representative Reynolds numbers are shown in Figures 12 and 13. In Figure 12, for both Reynolds numbers, the blunt tip case exhibits a clear stagnation region with low velocity magnitude near the tip of the rod. In contrast, the cone tip shapes show limited stagnation regions, which can be attributed to their more streamlined shape. In fact, the streamlined shape of the cones helps mitigate flow separation at the geometric transition near the edge of the rod tip. Figure 13 provides further insights into the flow behaviour. In the upstream region, below the rod free end, the flow exhibits a fully developed pipe flow pattern, characterized by aligned parallel streamlines to the pipe axis. For the blunt tip shape, distinct separation bubbles characterized by significant vorticity magnitudes manifest on both sides of the rod. These flow separation regions are significantly reduced when cone tip shapes are employed, and the extent of separation decreases with the increase of the cone height-to-diameter ratio.

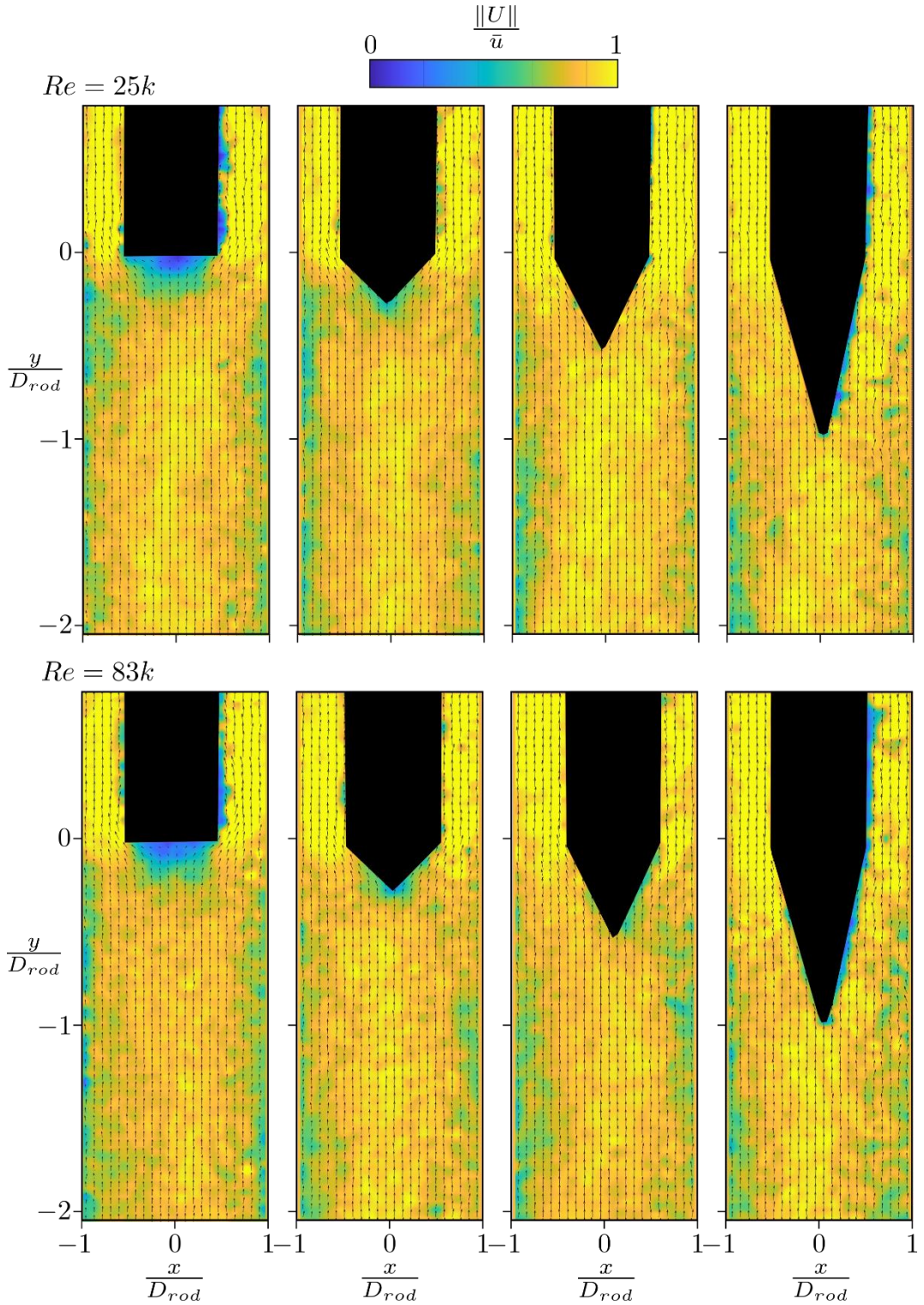

Figure 12. Velocity magnitude normalized with respect to the mean flow velocity within the annular gap, $\bar{u}$, for different tip shapes at Reynolds number of 25k and 83k. Quiver vectors indicate velocity field.

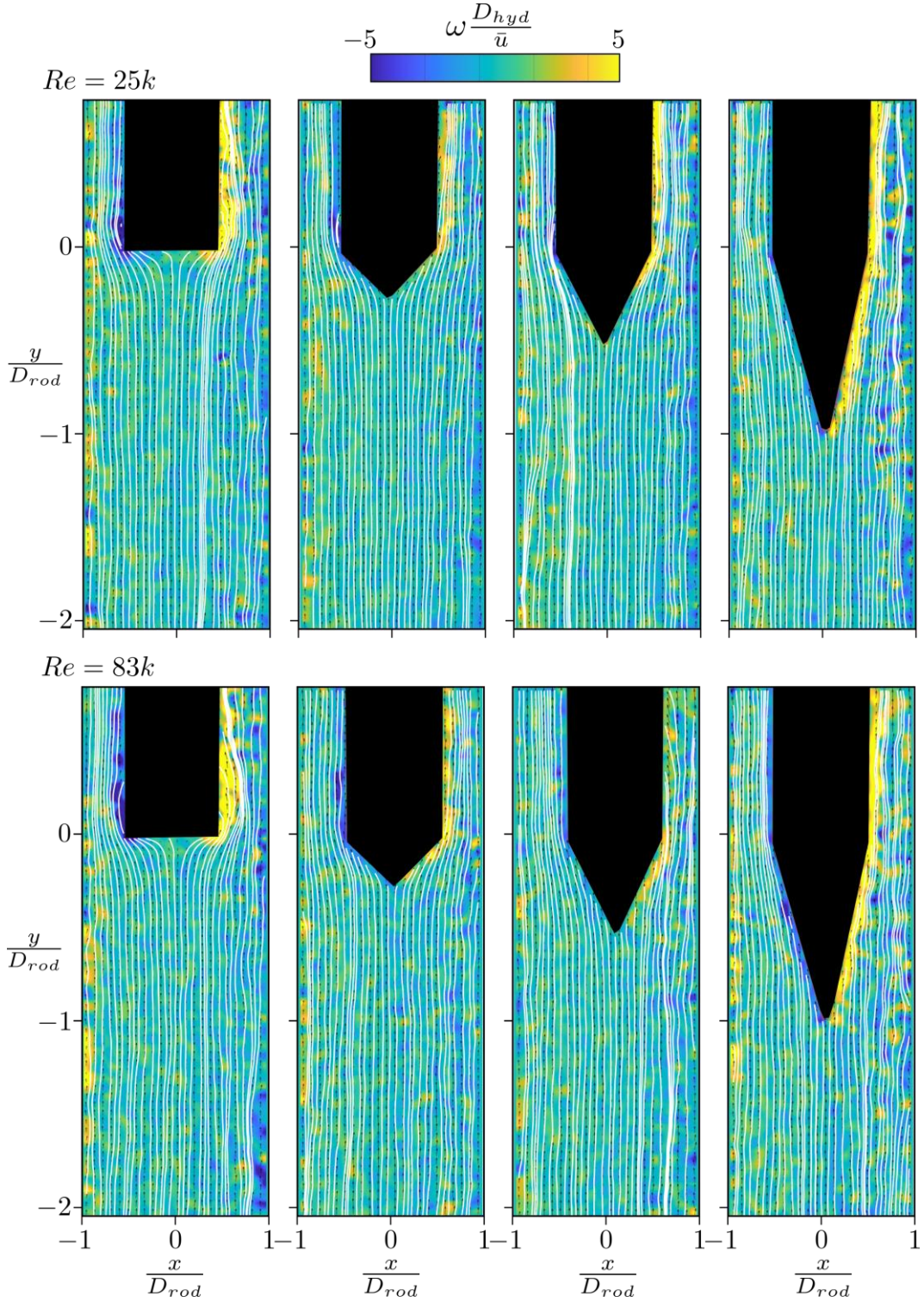

Figure 13. Vorticity and streamline for different tip shapes at Reynolds number of 25k and 83k. Vorticity, ω, is obtained by taking the curl of the velocity field.

At low Reynolds numbers, turbulent buffeting is identified as the main excitation mechanism for flow-induced vibration in this configuration. This observation aligns with the rod vibration dynamics, where the motion exhibits a chaotic nature with a periodic component, referred to

as fuzzy period-1, as shown in Figure A5 – A8. It is noteworthy that for the free-clamped configuration, flow separation bubbles are observed only for the blunt tip rod, whereas all the cone tip shapes exhibit minimal flow separation. This contrasts with the clamped-free configuration, where unsteady flow separation was only suppressed for the cone tip shape with h/d = 2 at low Reynolds numbers. As the vibration displacement increases, it is expected that the flow separation bubbles near the blunt-tipped rod, as depicted in Figure 13, will tend to develop into vortices and shed downstream on either side of the edges, depending on the deflection direction of the rod. Clearly, the separation bubbles near the blunt rod tip contribute to additional excitation of rod vibrations, resulting in a larger RMS displacement for the blunt tip rod compared to the cone tip rods at low Reynolds numbers, as illustrated in Figure 10. However, as the Reynolds number increases, movement-induced vibration becomes more pronounced, and the periodic component of rod vibration gains greater importance. With movement-induced excitation taking over the dominance as the primary excitation mechanism, the difference in RMS displacement between the blunt tip rod and cone tip shapes tends to diminish.

4. Concluding Remarks

This study experimentally investigated the influence of the tip shape on the vibration dynamics of a slender cantilever rod subjected to axial water flow. Its original contribution is in the demonstration and explanation of how different tip shapes affect the vibration of a cantilever rod, driven by axial flow. This is accomplished through optical tracking of the rod vibrations and detailed mapping of the flow field around the rod tips. The tip shapes considered in the study included a blunt shape and cone shapes with different height-to-diameter ratios. Two different configurations, namely the clamped-free configuration and the free-clamped configuration, of the cantilever rod have been investigated. The experiments have been conducted across a range of Reynolds numbers between 20k and 100k.

At low Reynolds numbers, the primary motion of the rod for all tip shapes is characterized as fuzzy period-1, which refers to a periodic motion with a chaotic component. This behavior is observed in both the clamped-free and free-clamped configurations. As the Reynolds number increases, additional phenomena such as flutter-like oscillation in the clamped-free configuration and buckling in the free-clamped configuration are also observed.

In addition to the well-known flow excitation mechanisms of turbulent buffeting and movement-induced excitations, unsteady flow separation was found to have a significant influence on the rod vibration dynamics, with a relative importance that depends on the shape of the rod tip and the direction of the flow. In the clamped-free configuration, at low Reynolds numbers,

unsteady flow separation acts as an additional source of flow excitation to the rod tip. In this case, cone tip shapes with larger height-to-diameter ratios result in a larger surface area interacting with the wake vortices, leading to increased rod vibration displacements. However, at high Reynolds numbers, unsteady flow separation tends to weaken the effect of movement-induced excitation, resulting in reduced fluid forces acting on the rod surface. As a result, the blunt tip with separated flow is less sensitive to movement-induced excitations, whereas the cone tip with less flow separation is more influenced by movement-induced excitations. This results in a larger vibration displacement and ultimately flutter divergence of the rod. In the free-clamped configuration, unsteady flow separation was found to provide additional flow excitation to rod vibrations. As a result, the blunt tip with a larger flow separation leads to larger vibration displacement compared to the cone tips. However, with the increase of Reynolds number, movement-induced excitations become more significant, and the displacements of the blunt tip and cone tips tend to equalize.

The findings of this study contribute to an improved understanding of the fluid-structure interaction mechanisms underlying axial-flow-induced vibrations of slender cantilever rods. These insights are valuable for the design of slender structures in axial flow, such as nuclear fuel rods, and for the mitigation and control of flow-induced vibrations in practical applications. Furthermore, the study provides data that can be used to develop and validate numerical approaches for simulating fluid-structure interactions.

Appendix A

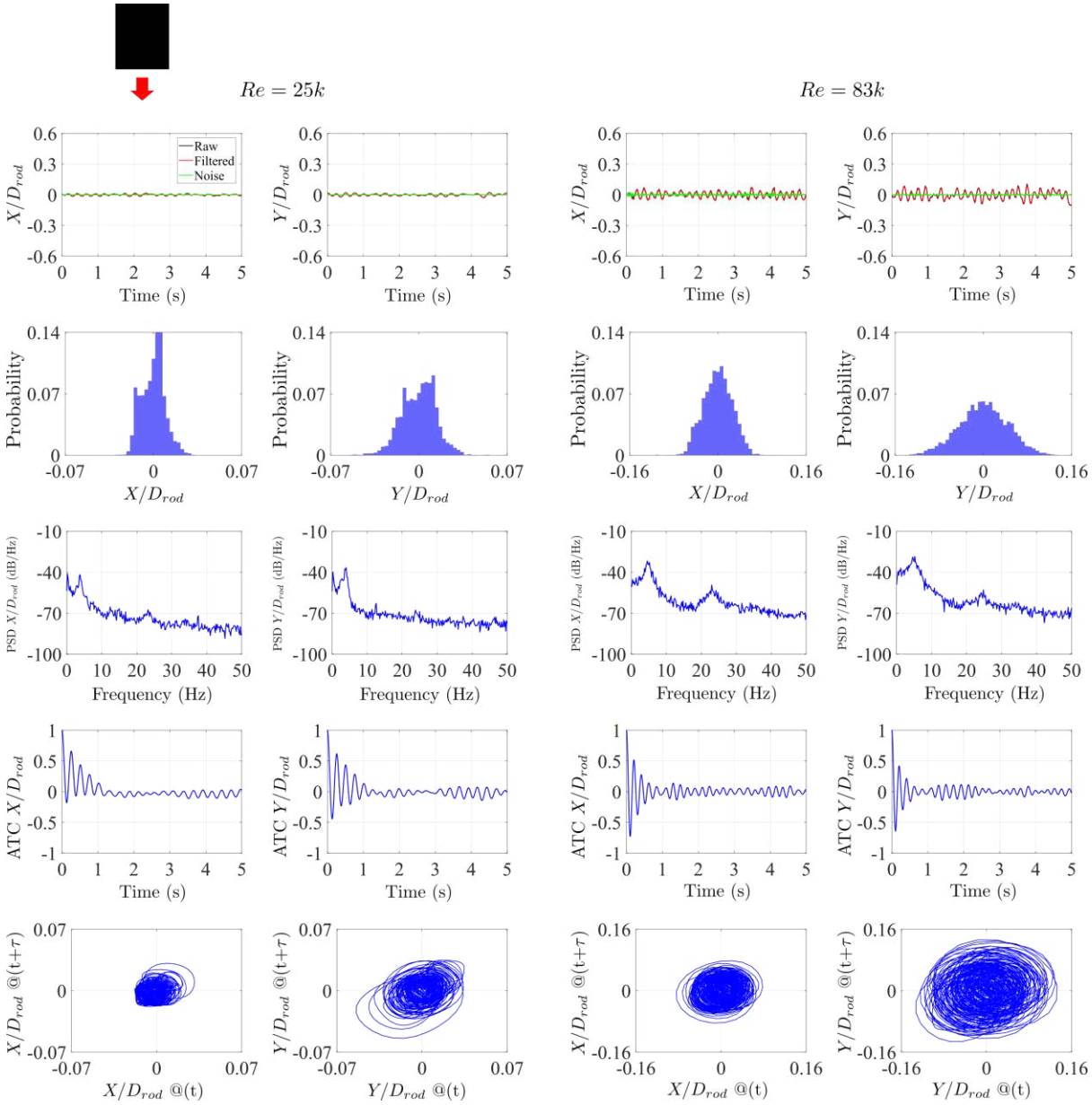

Figure A1. Displacement time series, histogram, PSD, autocorrelation function and phase-space topology for rod with blunt tip shape at Reynolds number of 25k and 83k for the clamped-free configuration.

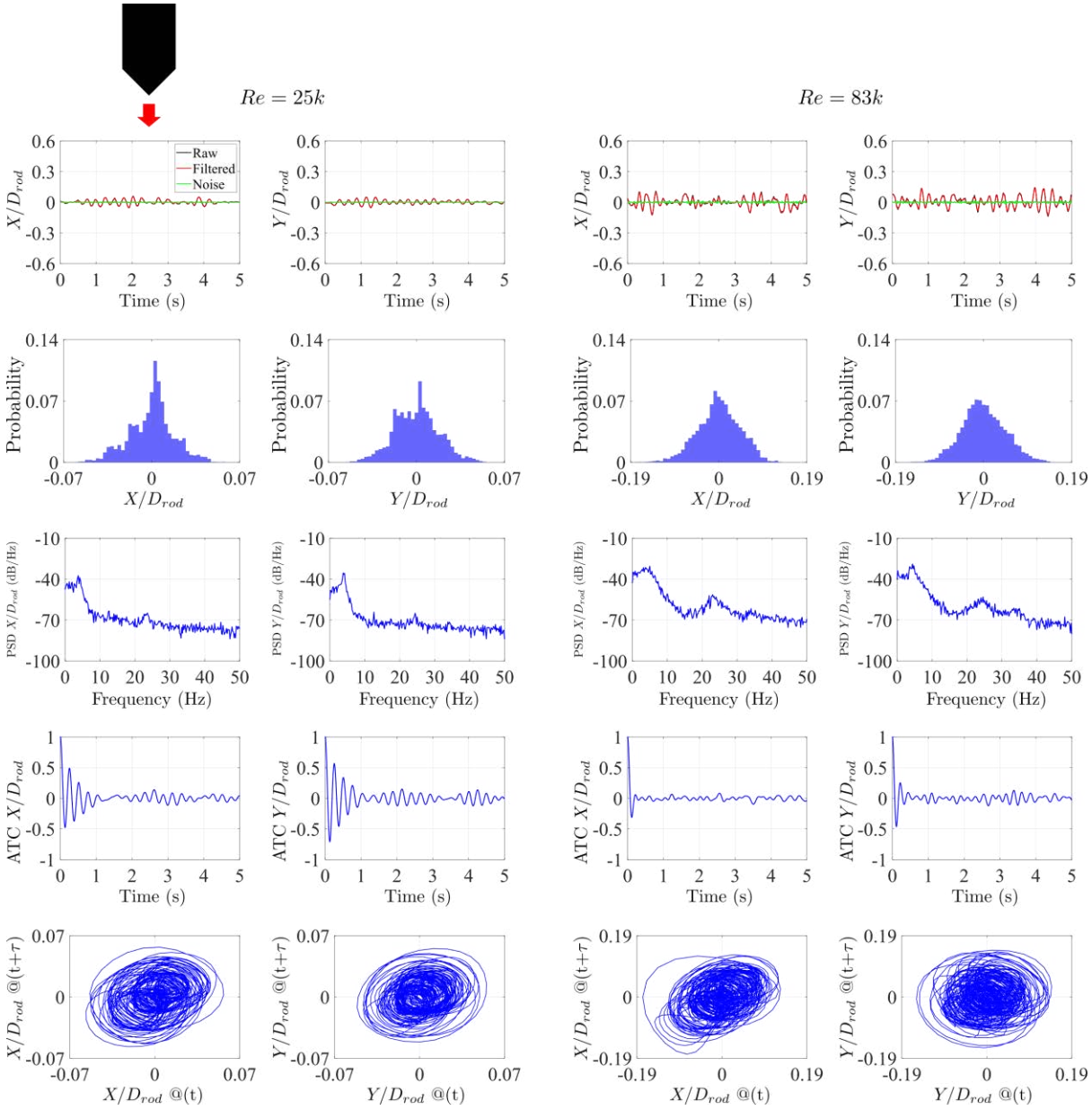

Figure A2. Displacement time series, histogram, PSD, autocorrelation function and phase-space topology for rod with h/d = 0.5 cone tip shape at Reynolds number of 25k and 83k for the free-clamped configuration.

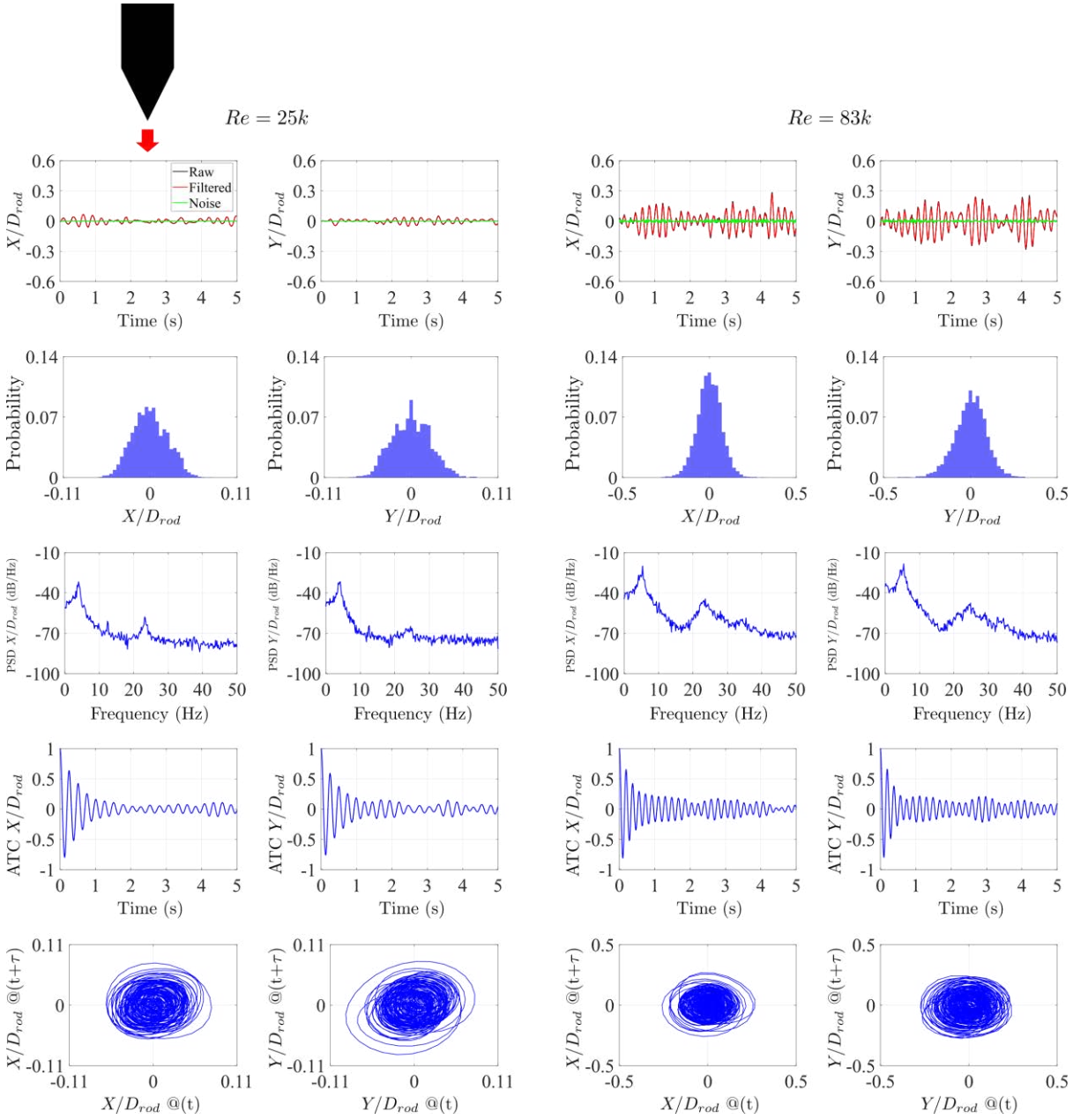

Figure A3. Displacement time series, histogram, PSD, autocorrelation function and phase-space topology for rod with h/d = 1.0 cone tip shape at Reynolds number of 25k and 83k for the free-clamped configuration.

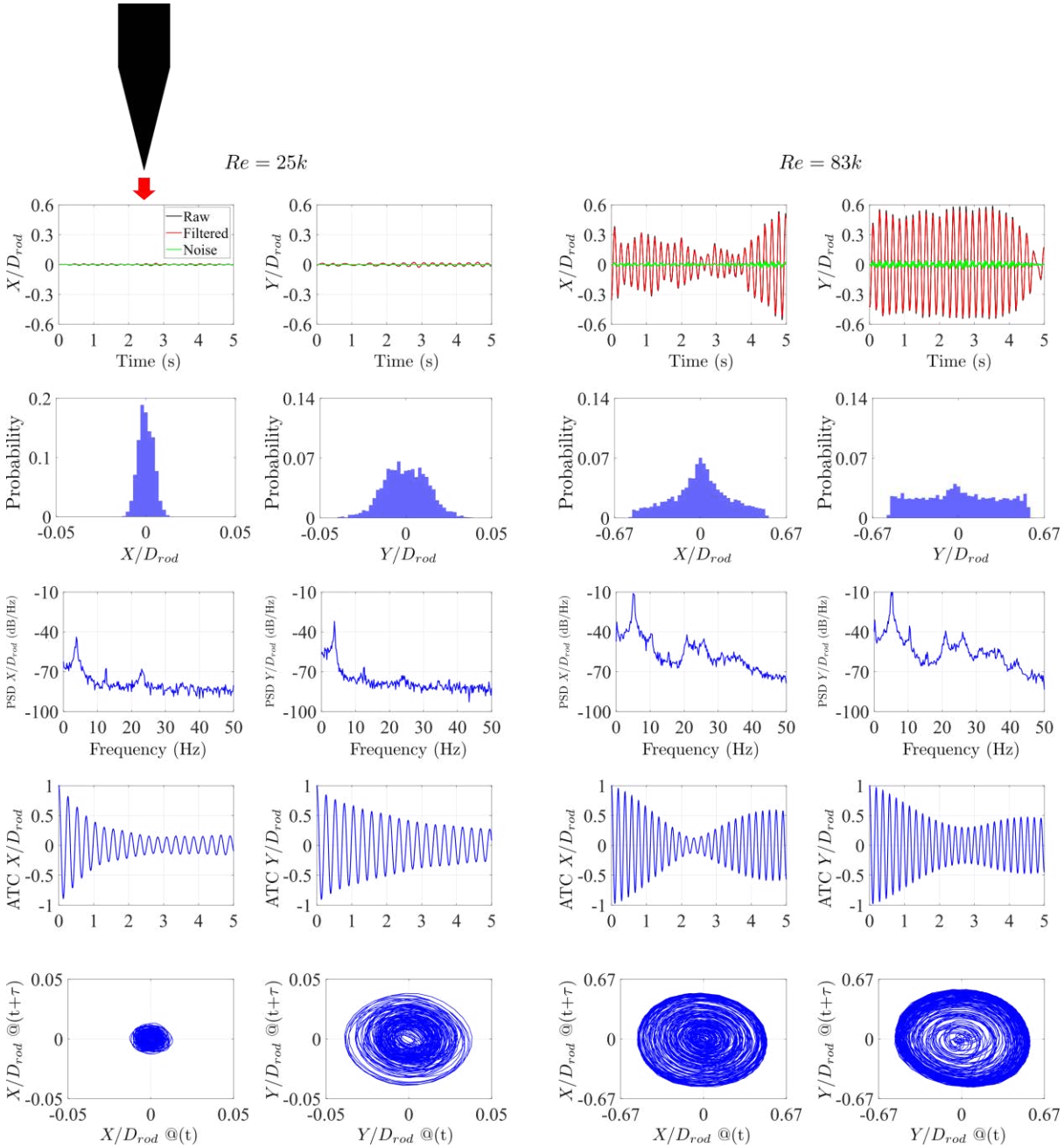

Figure A4. Displacement time series, histogram, PSD, autocorrelation function and phase-space topology for rod with h/d = 2.0 cone tip shape at Reynolds number of 25k and 83k for the free-clamped configuration.

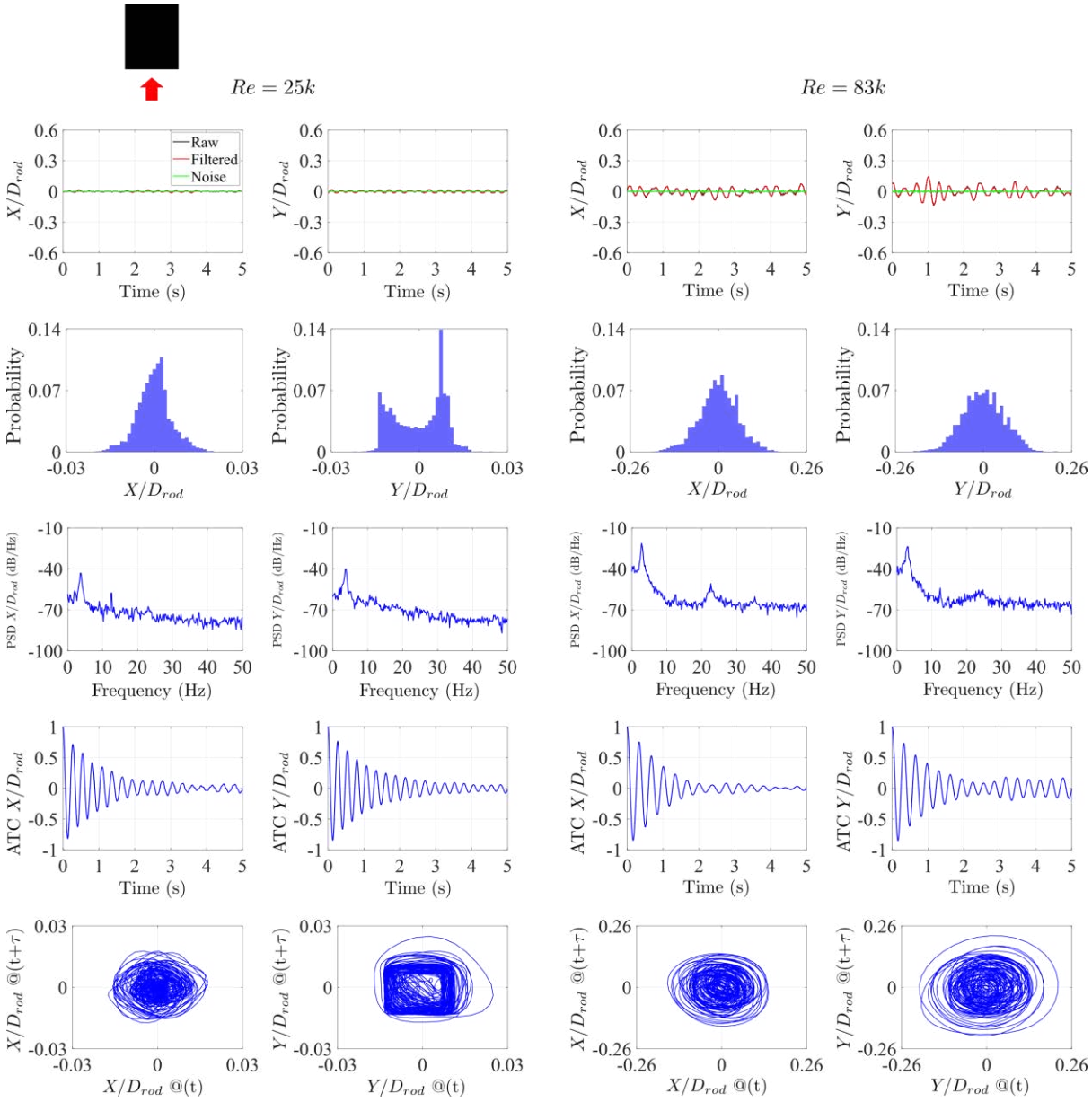

Figure A5. Displacement time series, histogram, PSD, autocorrelation function and phase-space topology for rod with blunt tip shapes at Reynolds number of 25k and 83k for the clamped-free configuration.

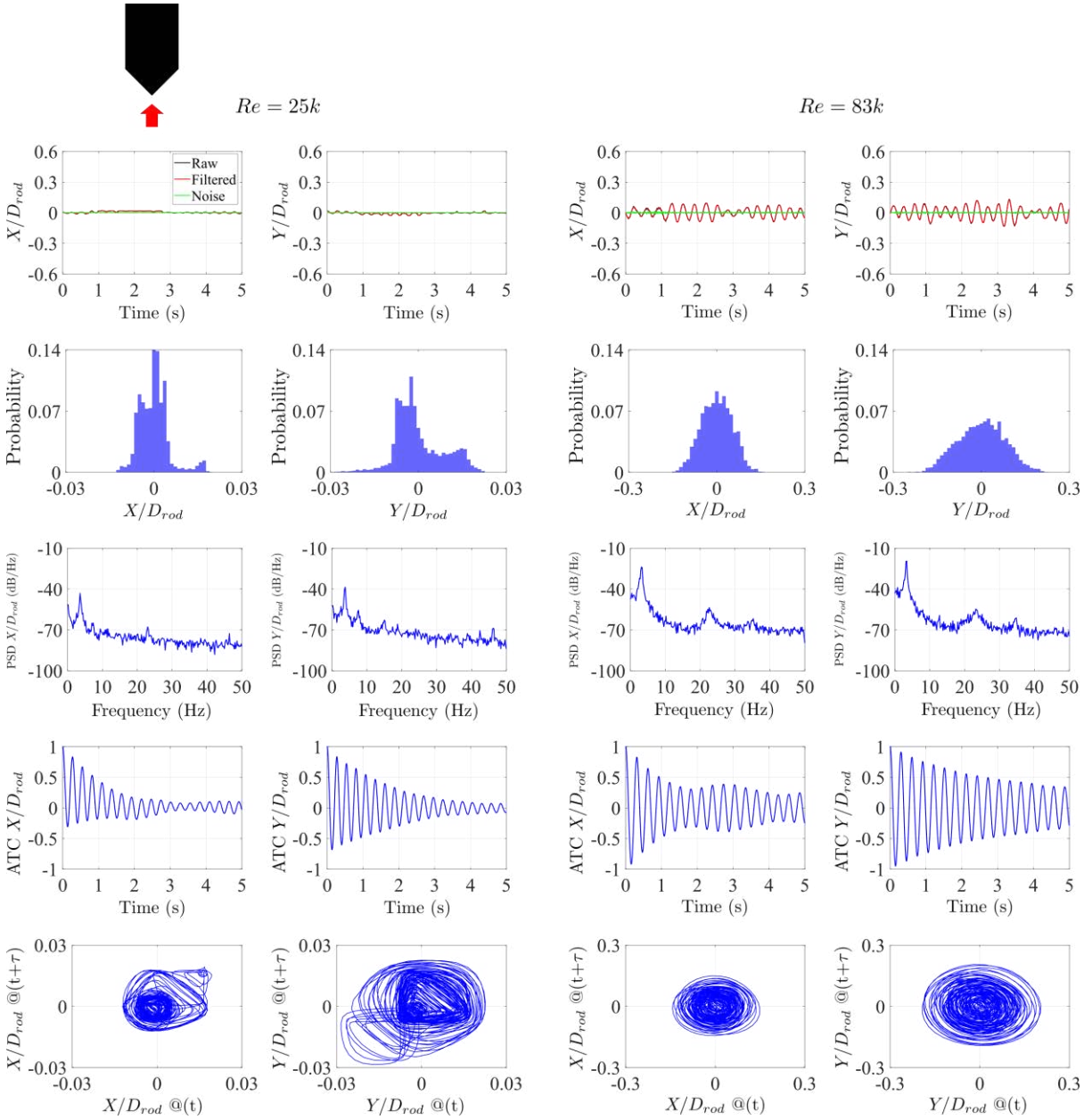

Figure A6. Displacement time series, histogram, PSD, autocorrelation function and phase-space topology for rod with h/d = 0.5 cone tip shape at Reynolds number of 25k and 83k for the clamped-free configuration.

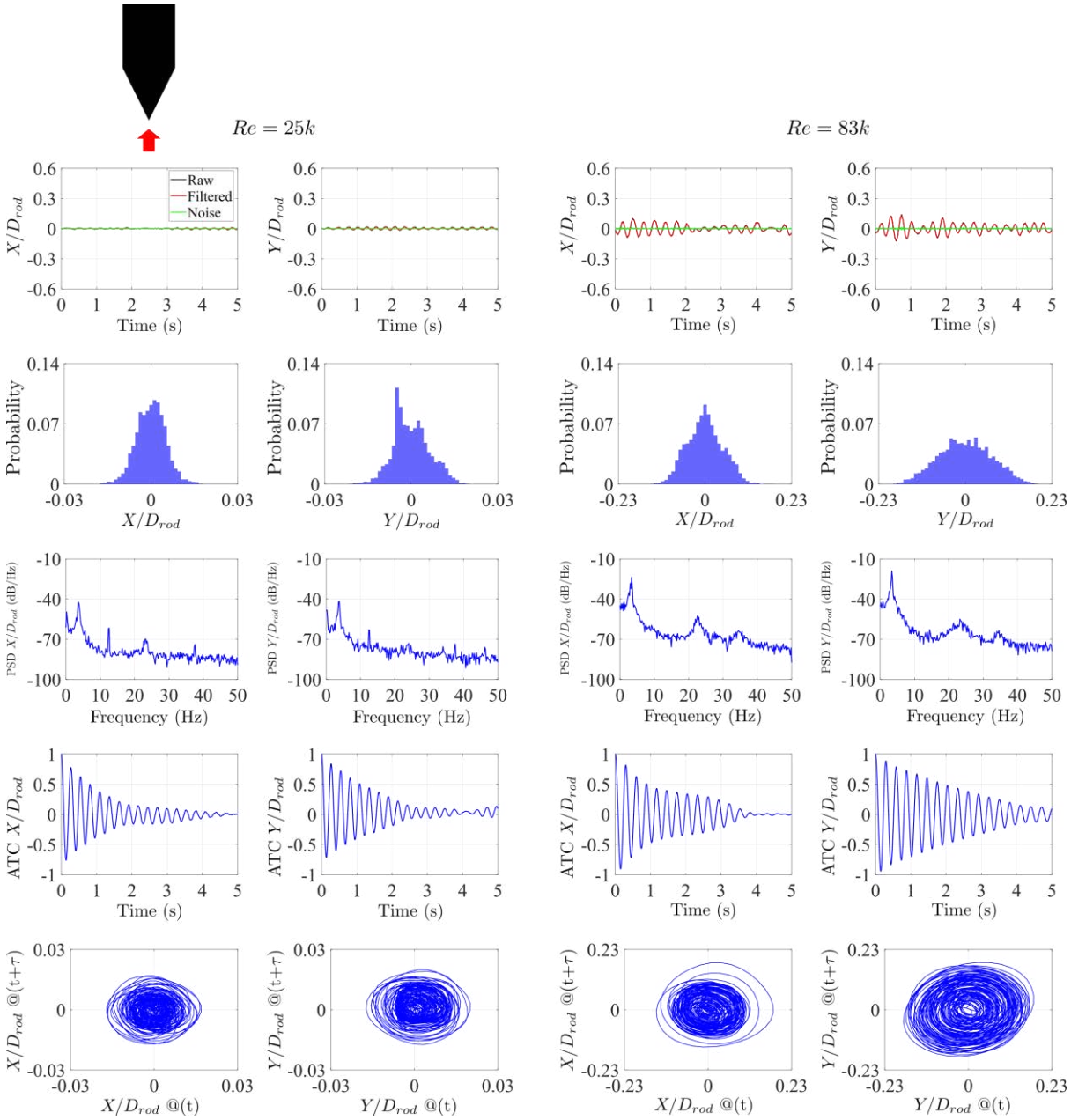

Figure A7. Displacement time series, histogram, PSD, autocorrelation function and phase-space topology for rod with h/d = 1.0 cone tip shape at Reynolds number of 25k and 83k for the clamped-free configuration.

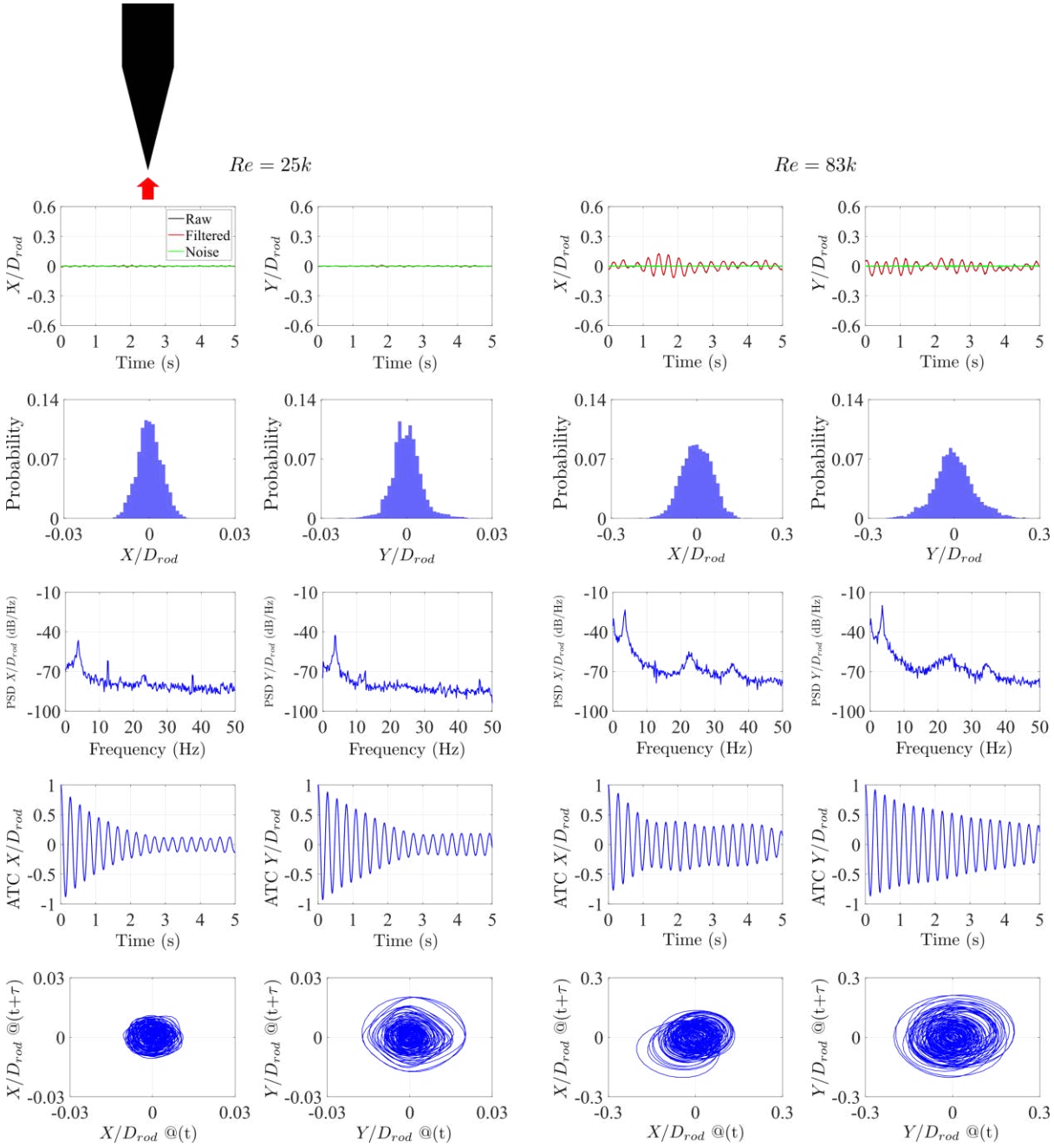

Figure A8. Displacement time series, histogram, PSD, autocorrelation function and phase-space topology for rod with h/d = 2.0 cone tip shape at Reynolds number of 25k and 83k for the clamped-free configuration.

Acknowledgments

This work was performed within the European GO-VIKING Horizon project (Grant Agreement 101060826) and was funded by UK Research and Innovation (UKRI) under the UK Government's Horizon Europe funding guarantee (Grant Number 10058366). The support of EDF (France) and EDF-Energy (UK) is gratefully acknowledged.

References

1. Triantafyllou, M.S.; Triantafyllou, G.S.; Yue, D.K.P. Hydrodynamics of Fishlike Swimming. *Annu. Rev. Fluid Mech.* **2000**, *32*, 33–53, doi:10.1146/annurev.fluid.32.1.33.
2. Matsumoto, M.; Daito, Y.; Kanamura, T.; Shigemura, Y.; Sakuma, S.; Ishizaki, H. Wind-Induced Vibration of Cables of Cable-Stayed Bridges. *Journal of Wind Engineering and Industrial Aerodynamics* **1998**, *74–76*, 1015–1027, doi:10.1016/S0167-6105(98)00093-2.
3. Chung, J.S.; Whitney, A.K.; Loden, W.A. Nonlinear Transient Motion Of Deep Ocean Mining Pipe.; May 5 1980; p. OTC-3832-MS.
4. Païdoussis, M.P.; Abdelbaki, A.R.; Butt, M.F.J.; Tavallaeinejad, M.; Moditis, K.; Misra, A.K.; Nahon, M.; Ratigan, J.L. Dynamics of a Cantilevered Pipe Subjected to Internal and Reverse External Axial Flow: A Review. *Journal of Fluids and Structures* **2021**, *106*, 103349, doi:10.1016/j.jfluidstructs.2021.103349.
5. Singh, K.; Michelin, S.; De Langre, E. Energy Harvesting from Axial Fluid-Elastic Instabilities of a Cylinder. *Journal of Fluids and Structures* **2012**, *30*, 159–172, doi:10.1016/j.jfluidstructs.2012.01.008.
6. Borsoi, L. Flow-Induced Vibration of Nuclear Components: Future R&D Perspective Derived from the French Experience.
7. Cioncolini, A.; Silva-Leon, J.; Cooper, D.; Quinn, M.K.; Iacovides, H. Axial-Flow-Induced Vibration Experiments on Cantilevered Rods for Nuclear Reactor Applications. *Nuclear Engineering and Design* **2018**, *338*, 102–118, doi:10.1016/j.nucengdes.2018.08.010.
8. Cioncolini, A.; Zhang, S.; Nabawy, M.R.A.; Li, H.; Cooper, D.; Iacovides, H. Experiments on Axial-Flow-Induced Vibration of a Free-Clamped/Clamped-Free Rod for Light-Water Nuclear Reactor Applications. *Annals of Nuclear Energy* **2023**, *190*, 109900, doi:10.1016/j.anucene.2023.109900.
9. Salachna, J.; Cioncolini, A.; Iacovides, H. Benchmark Simulation of the Flow-Induced Vibrations for Nuclear Applications. *Ann. Nucl. Energy* **2023**, *180*, 109425, doi:10.1016/j.anucene.2022.109425.
10. *Review of Fuel Failures in Water Cooled Reactors*; Nuclear Energy Series; INTERNATIONAL ATOMIC ENERGY AGENCY: Vienna, 2010; ISBN 978-92-0-102610-1.
11. Cai, Z.; Li, Z.; Yin, M.; Zhu, M.; Zhou, Z. A Review of Fretting Study on Nuclear Power Equipment. *Tribology International* **2020**, *144*, 106095, doi:10.1016/j.triboint.2019.106095.
12. Shoei-sheng Chen; Wambsganss, M.W. Parallel-Flow-Induced Vibration of Fuel Rods. *Nuclear Engineering and Design* **1972**, *18*, 253–278, doi:10.1016/0029-5493(72)90144-6.
13. Païdoussis, M.P. Dynamics of Cylindrical Structures in Axial Flow: A Review. *Journal of Fluids and Structures* **2021**, *107*, 103374, doi:10.1016/j.jfluidstructs.2021.103374.
14. Paidoussis, M.P. Dynamics of Flexible Slender Cylinders in Axial Flow Part 2. Experiments. *J. Fluid Mech.* **1966**, *26*, 737–751, doi:10.1017/S0022112066001496.
15. Wambsganss, M.W.; Jendrzejczyk, J.A. The Effect of Trailing End Geometry on the Vibration of a Circular Cantilevered Rod in Nominally Axial Flow. *Journal of Sound and Vibration* **1979**, *65*, 251–258, doi:10.1016/0022-460X(79)90518-2.

16. Rinaldi, S.; Païdoussis, M.P. Theory and Experiments on the Dynamics of a Free-Clamped Cylinder in Confined Axial Air-Flow. *Journal of Fluids and Structures* **2012**, *28*, 167–179, doi:10.1016/j.jfluidstructs.2011.07.006.
17. De Santis, D.; Kottapalli, S.; Shams, A. Numerical Simulations of Rod Assembly Vibration Induced by Turbulent Axial Flows. *Nucl. Eng. Des.* **2018**, *335*, 94–105, doi:10.1016/j.nucengdes.2018.04.027.
18. De Santis, D.; Shams, A. Numerical Study of Flow-Induced Vibration of Fuel Rods. *Nucl. Eng. Des.* **2020**, *361*, 110547, doi:10.1016/j.nucengdes.2020.110547.
19. De Santis, D.; Shams, A. An Advanced Numerical Framework for the Simulation of Flow Induced Vibration for Nuclear Applications. *Ann. Nucl. Energy* **2019**, *130*, 218–231, doi:10.1016/j.anucene.2019.02.049.
20. Dolfen, H.; De Ridder, J.; Brockmeyer, L.; Merzari, E.; Kennedy, G.; Van Tichelen, K.; Degroote, J. A Multi-Stage Approach of Simulating Turbulence-Induced Vibrations in a Wire-Wrapped Tube Bundle for Fretting Wear Prediction. *J. Fluids Struct.* **2022**, *109*, 103460, doi:10.1016/j.jfluidstructs.2021.103460.
21. Je, S.Y.; Kim, H.-G.; Chang, Y.-S. Turbulent Flow Effect on Integrity of Pressurized RVIs. *Ann. Nucl. Energy* **2021**, *163*, 108564, doi:10.1016/j.anucene.2021.108564.
22. Liu, H.; Chen, D.; Hu, L.; Yuan, D.; Gao, H. Numerical Investigations on Flow-Induced Vibration of Fuel Rods with Spacer Grids Subjected to Turbulent Flow. *Nucl. Eng. Des.* **2017**, *325*, 68–77, doi:10.1016/j.nucengdes.2017.10.004.
23. ter Hofstede, E.; Kottapalli, S.; Shams, A. Numerical Prediction of Flow Induced Vibrations in Nuclear Reactor Applications. *Nucl. Eng. Des.* **2017**, *319*, 81–90, doi:10.1016/j.nucengdes.2017.04.026.
24. Wang, Y.; Zheng, M.; Zhang, J.; Jiao, Y.; Wu, Y.; Tian, W.; Su, G.H.; Qiu, S. Numerical Simulation Study on the Fluid Excitation Force on a Nuclear Fuel Rod with a Spacer Grid. *Ann. Nucl. Energy* **2023**, *180*, 109472, doi:10.1016/j.anucene.2022.109472.
25. Lemmon, E.; Huber, M.; McLinden, M. NIST Standard Reference Database 23: Reference Fluid Thermodynamic and Transport Properties-REFPROP, Version 9.1 2013.
26. Silva-Leon, J.; Cioncolini, A.; Filippone, A.; Domingos, M. Flow-Induced Motions of Flexible Filaments Hanging in Cross-Flow. *Experimental thermal and fluid science* **2018**, *97*, 254–269, doi:10.1016/j.expthermflusci.2018.04.023.
27. Cioncolini, A.; Nabawy, M.R.; Silva-Leon, J.; O'Connor, J.; Revell, A. An Experimental and Computational Study on Inverted Flag Dynamics for Simultaneous Wind–Solar Energy Harvesting. *Fluids (Basel)* **2019**, *4*, 87-, doi:10.3390/fluids4020087.
28. Silva-Leon, J.; Cioncolini, A.; Nabawy, M.R.; Revell, A.; Kennaugh, A. Simultaneous Wind and Solar Energy Harvesting with Inverted Flags. *Applied energy* **2019**, *239*, 846–858, doi:10.1016/j.apenergy.2019.01.246.
29. Yang, K.; Nabawy, M.R.A.; Cioncolini, A.; Revell, A.; AlGhrairy, S. Planform Geometry Effects of Piezoelectric Wind Energy Harvesting Composite Inverted Flags. *Smart materials and structures* **2021**, *30*, 115014-, doi:10.1088/1361-665X/ac2b8a.
30. Yang, K.; Cioncolini, A.; Nabawy, M.R.A.; Revell, A. Mechanical Durability Assessment of an Energy-Harvesting Piezoelectric Inverted Flag. *Energies (Basel)* **2021**, *15*, 77-, doi:10.3390/en15010077.
31. Eaton, J.W. *Gnu Octave 4.2 Reference Manual*; Samurai Media Limited: London, GBR, 2017; ISBN 978-988-8407-07-1.
32. Welch, P. The Use of Fast Fourier Transform for the Estimation of Power Spectra: A Method Based on Time Averaging over Short, Modified Periodograms. *IEEE Trans. Audio Electroacoust.* **1967**, *15*, 70–73, doi:10.1109/TAU.1967.1161901.
33. Henderson, R. Note on Graduation by Adjusted Average. *Transactions of the actuarial society of America* **1916**, *17*, 43–48.
34. Rogers, R.J.; Taylor, C.; Pettigrew, M.J. Fluid Effects on Multi-Span Heat Exchanger Tube Vibration. *ASME Journal of Pressure Vessel and Piping, ASME Publication H* **1984**, *316*, 17–26.

35. Thielicke, W.; Stamhuis, E.J. PIVlab – Towards User-Friendly, Affordable and Accurate Digital Particle Image Velocimetry in MATLAB. *Journal of Open Research Software* **2014**, *2*, doi:10.5334/jors.bl.
36. Paidoussis, M.P. *Fluid-Structure Interactions: Slender Structures and Axial Flow*; Academic press, 1998; Vol. 1; ISBN 0-08-053175-X.